

## GALACTIC GLOBULAR AND OPEN CLUSTERS IN THE SLOAN DIGITAL SKY SURVEY. I. CROWDED FIELD PHOTOMETRY AND CLUSTER FIDUCIAL SEQUENCES IN *ugriz*

DEOKKEUN AN<sup>1</sup>, JENNIFER A. JOHNSON<sup>1</sup>, JAMES L. CLEM<sup>2</sup>, BRIAN YANNY<sup>3</sup>, CONSTANCE M. ROCKOSI<sup>4</sup>,  
HEATHER L. MORRISON<sup>5</sup>, PAUL HARDING<sup>5</sup>, JAMES E. GUNN<sup>6</sup>, CARLOS ALLENDE PRIETO<sup>7</sup>,  
TIMOTHY C. BEERS<sup>8</sup>, KYLE M. CUDWORTH<sup>9</sup>, INESE I. IVANS<sup>6,10</sup>, ŽELJKO IVEZIĆ<sup>11</sup>,  
YOUNG SUN LEE<sup>8</sup>, ROBERT H. LUPTON<sup>6</sup>, DMITRY BIZYAEV<sup>12</sup>, HOWARD BREWINGTON<sup>12</sup>,  
ELENA MALANUSHENKO<sup>12</sup>, VIKTOR MALANUSHENKO<sup>12</sup>, DAN ORAVETZ<sup>12</sup>,  
KAIKE PAN<sup>12</sup>, AUDREY SIMMONS<sup>12</sup>, STEPHANIE SNEDDEN<sup>12</sup>,  
SHANNON WATTERS<sup>12</sup>, AND DONALD G. YORK<sup>13,14</sup>

*Accepted for publication in ApJS*

### ABSTRACT

We present photometry for globular and open cluster stars observed with the Sloan Digital Sky Survey (SDSS). In order to exploit over 100 million stellar objects with  $r < 22.5$  mag observed by SDSS, we need to understand the characteristics of stars in the SDSS *ugriz* filters. While star clusters provide important calibration samples for stellar colors, the regions close to globular clusters, where the fraction of field stars is smallest, are too crowded for the standard SDSS photometric pipeline to process. To complement the SDSS imaging survey, we reduce the SDSS imaging data for crowded cluster fields using the DAOPHOT/ALLFRAME suite of programs and present photometry for 17 globular clusters and 3 open clusters in a SDSS value-added catalog. Our photometry and cluster fiducial sequences are on the native SDSS 2.5-meter *ugriz* photometric system, and the fiducial sequences can be directly applied to the SDSS photometry without relying upon any transformations. Model photometry for red giant branch and main-sequence stars obtained by Girardi et al. cannot be matched simultaneously to fiducial sequences; their colors differ by  $\sim 0.02$ – $0.05$  mag. Good agreement ( $\lesssim 0.02$  mag in colors) is found with Clem et al. empirical fiducial sequences in  $u'g'r'i'z'$  when using the transformation equations in Tucker et al.

*Subject headings:* globular clusters: general — Hertzsprung–Russell diagram — open clusters and associations: general — stars: evolution — Surveys

### 1. INTRODUCTION

As single-age and (in most cases) single-metallicity populations, Galactic star clusters provide important calibration samples for exploring the relationships between stellar colors and absolute magnitudes as functions of stellar age and heavy-element content. These two observable properties of a star are related to fundamental physical parameters, such as the effective

temperature ( $T_{\text{eff}}$ ) and surface gravity ( $\log g$ ), as well as the metallicity. The color and magnitude relations can be used to test stellar evolutionary theories, to interpret the observed distribution of stars in color-color and color-magnitude diagrams (CMDs), and to derive distances to stars and star clusters via photometric parallax or main-sequence (MS) fitting techniques (e.g., Johnson 1957).

Because the relationships between magnitude, color, and fundamental stellar properties depend on the filters used, it is necessary to characterize these relations for each filter system. Galactic globular and open clusters provide an ideal opportunity to achieve this goal because the same distance can be assumed for cluster members with a wide range of stellar masses. Furthermore, observations of a large number of Galactic clusters can cover a wide range of the heavy-element content, providing an opportunity to explore the effects of metallicity on magnitudes and colors for each set of filter bandpasses.

Among previous and ongoing optical surveys, the Sloan Digital Sky Survey (SDSS; York et al. 2000; Stoughton et al. 2002; Abazajian et al. 2003, 2004, 2005; Adelman-McCarthy et al. 2006, 2007, 2008) is the largest and most homogeneous database of stellar brightnesses currently available. The original goal of the SDSS was to survey large numbers of galaxies and quasars. However, in the first five years of operation, SDSS-I has made remarkable contributions to our understanding of the Milky Way and its stellar populations (e.g., Newberg et al. 2002; Allende Prieto et al. 2006; Belokurov et al. 2006; de Jong et al. 2008; Jurić et al. 2008). These successes have initiated the Galactic structure program SEGUE (Sloan Extension for Galactic Understand-

<sup>1</sup> Department of Astronomy, Ohio State University, 140 West 18th Avenue, Columbus, OH 43210; deokkeun.jaj@astronomy.ohio-state.edu.

<sup>2</sup> Department of Physics & Astronomy, Louisiana State University, 202 Nicholson Hall, Baton Rouge, LA 70803.

<sup>3</sup> Fermi National Accelerator Laboratory, P.O. Box 500, Batavia, IL 60510.

<sup>4</sup> UCO/Lick Observatory, University of California, Santa Cruz, CA 95064.

<sup>5</sup> Department of Astronomy, Case Western Reserve University, Cleveland, OH 44106.

<sup>6</sup> Department of Astrophysical Sciences, Princeton University, Princeton, NJ 08544.

<sup>7</sup> McDonald Observatory and Department of Astronomy, The University of Texas, 1 University Station, C1400, Austin, TX 78712-0259.

<sup>8</sup> Department of Physics & Astrophysics, CSCE: Center for the Study of Cosmic Evolution, and JINA: Joint Institute for Nuclear Astrophysics, Michigan State University, E. Lansing, MI 48824.

<sup>9</sup> Yerkes Observatory, University of Chicago, 373 West Geneva Street, Williams Bay, WI 53191.

<sup>10</sup> The Observatories of the Carnegie Institution of Washington, 813 Santa Barbara St., Pasadena, CA 91101.

<sup>11</sup> Department of Astronomy, University of Washington, Box 351580, Seattle, WA 98195.

<sup>12</sup> Apache Point Observatory, P.O. Box 59, Sunspot, NM 88349.

<sup>13</sup> Department of Astronomy and Astrophysics, University of Chicago, 5640 South Ellis Avenue, Chicago, IL 60637.

<sup>14</sup> Enrico Fermi Institute, University of Chicago, 5640 South Ellis Avenue, Chicago, IL 60637.

ing and Exploration; B. Yanny et al. 2008, in preparation), one of the surveys being conducted in the ongoing three year extension of the survey (SDSS-II). When SDSS-II finishes, it will provide imaging data for approximately 10,000 square degrees of the northern sky.

SDSS measures the brightnesses of stars using a dedicated 2.5-m telescope (Gunn et al. 2006) in five broad-band filters  $u$ ,  $g$ ,  $r$ ,  $i$ , and  $z$ , with average wavelengths of 3551Å, 4686Å, 6165Å, 7481Å, and 8931Å, respectively (Fukugita et al. 1996; Stoughton et al. 2002). The 95% detection repeatability limits are 22.0 mag, 22.2 mag, 22.2 mag, 21.3 mag, and 20.5 mag for point sources in  $u$ ,  $g$ ,  $r$ ,  $i$ , and  $z$ , respectively. The rms photometric precision is 0.02 mag for sources not limited by photon statistics (Ivezić et al. 2003), and the photometric calibration is accurate to  $\sim 2\%$  in the  $g$ ,  $r$ ,  $i$  bands, and  $\sim 3\%$  in  $u$  and  $z$  (Ivezić et al. 2004). The SDSS filters represent a new filter set for stellar observations, and therefore it is important to understand the properties of stars in this system. Furthermore, future imaging surveys such as the Panoramic Survey Telescope & Rapid Response System (Pan-STARRS; Kaiser et al. 2002) and the Large Synoptic Survey Telescope (LSST; Stubbs et al. 2004) will use similar photometric bandpasses, providing even deeper data in  $ugriz$  than SDSS over a larger fraction of the sky.

During the course of SDSS-I, about 15 globular clusters and several open clusters were observed. Several more clusters were imaged in SDSS-II including M71. These clusters together provide accurate calibration samples for stellar colors and magnitudes in the SDSS filters. The SDSS images are processed using the standard SDSS photometric pipelines (*Photo*; Lupton et al. 2002). *Photo* pre-processes the raw images, determines the point spread function (PSF), detects objects, and measures their properties. Photometric calibration is then carried out using observations of stars in the secondary patch transfer fields (Tucker et al. 2006; Davenport et al. 2007). In this paper, we simply refer to these calibrated magnitudes as *Photo* magnitudes.

*Photo* was originally designed to handle high Galactic latitude fields with relatively low densities of Galactic field stars (owing to the primarily extragalactic mission of SDSS-I); however, there are some concerns about its photometry derived in crowded fields (Adelman-McCarthy et al. 2008). In particular, stellar clusters present a challenge to *Photo*. Firstly, *Photo* slows down dramatically in the high density cluster cores, which are too crowded for *Photo* to process, so it does not provide photometry for the most crowded regions of these scans. Figure 1 compares a CMD for the globular cluster M3 obtained from *Photo* photometry to that obtained from a DAOPHOT (Stetson 1987) reduction in this paper, which is specifically designed for crowded field photometry. The *Photo* photometry is only available on the outskirts of the cluster, and it provides a considerably less well-defined sub-giant branch (SGB), red giant branch (RGB), and horizontal branch (HB). Secondly, there is a concern that the photometry in the area surrounding clusters, and in low Galactic latitude fields, may also be affected by inaccurate modeling of the PSF if stars in crowded regions were selected as PSF stars by *Photo*.

Photometric information in crowded fields can be extracted from the original SDSS imaging data. For example, Smolčić et al. (2007) used the DoPHOT (Schechter et al. 1993) photometry package to explore the structure of the Leo I dwarf spheroidal galaxy (dSph). Similarly,

Coleman et al. (2007) used the DAOPHOT package to study the stellar distribution of the dSph Leo II. In this paper, we employ the DAOPHOT/ALLFRAME (Stetson 1987, 1994) suite of programs to derive photometry for 17 globular clusters and 3 open clusters that have been observed with SDSS. We derive photometry by running DAOPHOT for SDSS imaging frames where *Photo* did not run. In addition, we reduce imaging data for fields farther away from the clusters, where the *Photo* results are expected to be reliable, in order to set up photometric zero points for the DAOPHOT photometry. We also compare DAOPHOT and *Photo* results for the open cluster fields to verify the accuracy of the *Photo* magnitudes in these semi-crowded fields.

An overview of the SDSS imaging survey and our sample clusters are presented in § 2. In § 3 we describe the preparation of imaging data from the SDSS database. In § 4 we describe the method of crowded field photometry using DAOPHOT/ALLFRAME, and evaluate the photometric accuracy. In § 5 we present cluster photometry and fiducial sequences, and compare them with theoretical stellar isochrones and fiducial sequences in  $u'g'r'i'z'$ .

## 2. SDSS OBSERVATIONS OF GALACTIC CLUSTERS

The SDSS images are taken in drift-scan or time-delay-and-integrate (TDI) mode, with an effective exposure time of 54.1 seconds per band. The imaging is carried out on moonless nights of good seeing (better than  $1.6''$ ) under photometric conditions (Hogg et al. 2001). A portion of the sky (along great circles) is imaged in each run by 6 columns of CCDs (Gunn et al. 1998). Each CCD observes  $13.52'$  of sky, forming a scanline or camcol, with a gap of  $11.68'$  between the columns. A second scan or strip in a different run fills in the gap, overlapping the first scan by 8% on each side (York et al. 2000). An example of the scanning pattern is shown in Figure 2 for the globular cluster M3. Each of the rectangular regions represent a SDSS field. Frames reduced in this paper are indicated as thick boxes.

Table 1 lists our sample of globular clusters observed by SDSS, and summarizes estimates of the reddening, distance moduli, and metallicity measurements for these clusters reported in the recent literature. A number of the properties are taken from the catalog of Harris (1996, February 2003 revision). We also include the  $[\text{Fe}/\text{H}]$  values reported by Kraft & Ivans (2003, 2004). These are based on Fe II lines from high-resolution spectra, which are expected to be less affected by non-local thermodynamic equilibrium (non-LTE) effects. In their study a consistent technique was employed to derive metallicities for giants in 16 key well-known globular clusters. Seven clusters in our sample are included in their sample of 16 key clusters. For the remaining sample clusters we list their  $[\text{Fe}/\text{H}]$  determinations based on the correlation between  $[\text{Fe}/\text{H}]_{\text{II}}$  and the reduced strength of the near-infrared Ca II triplet. Although these accurate metallicities make Galactic clusters useful calibrators, some of the lighter elements (always C and N, but sometimes also O, Na, Mg, and Al as well) vary from star to star (e.g., Kraft 1994). However, extensive studies have shown that the abundances of most elements (in particular Fe) are the same for all cluster stars (in the sample we consider), and the overall effect on the colors of stars in broadband filters, such as  $ugriz$ , from variations of these lighter elements should be small.

The distances and reddenings to clusters have also been the subject of much research. Kraft & Ivans used the *Hipparcos* subdwarfs (see references therein for their sample selection)

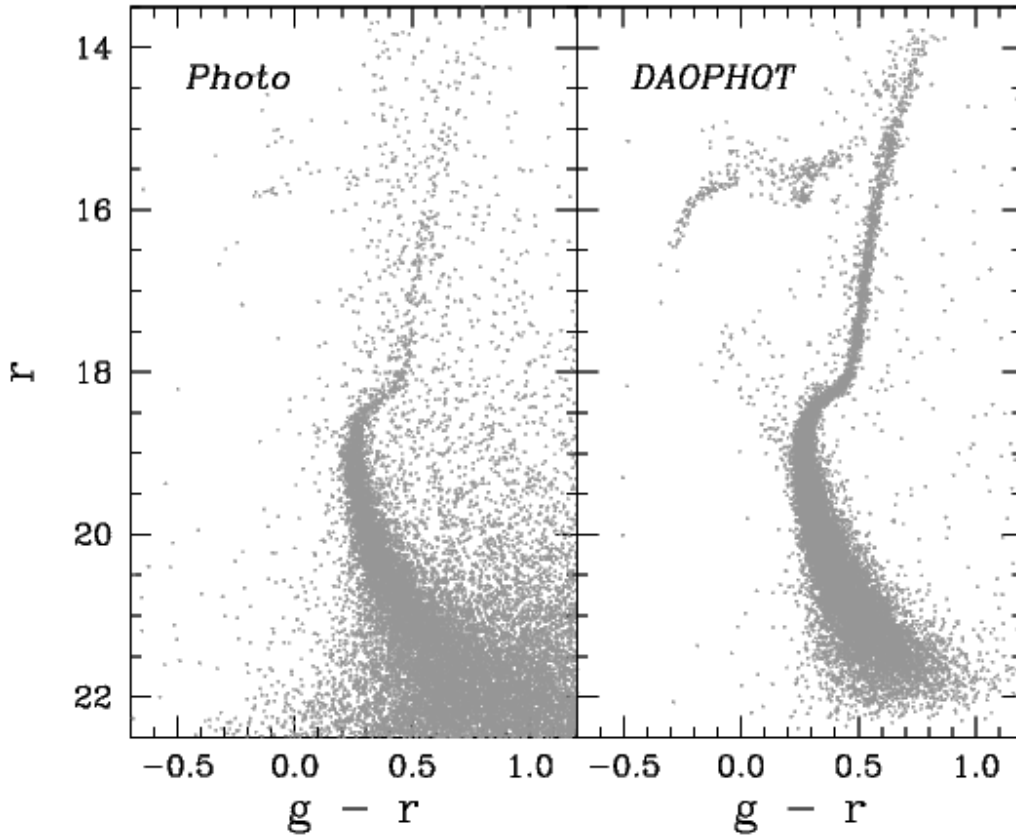


FIG. 1.— CMDs of M3 from the SDSS photometric pipeline (*Photo*; left) and DAOPHOT reduction in this paper (*right*). Stars within a  $30'$  radius from the cluster center are shown in the left panel, but the *Photo* photometry is only available on the outskirts of the cluster. In the right panel, RR Lyraes are scattered off the cluster horizontal branch.

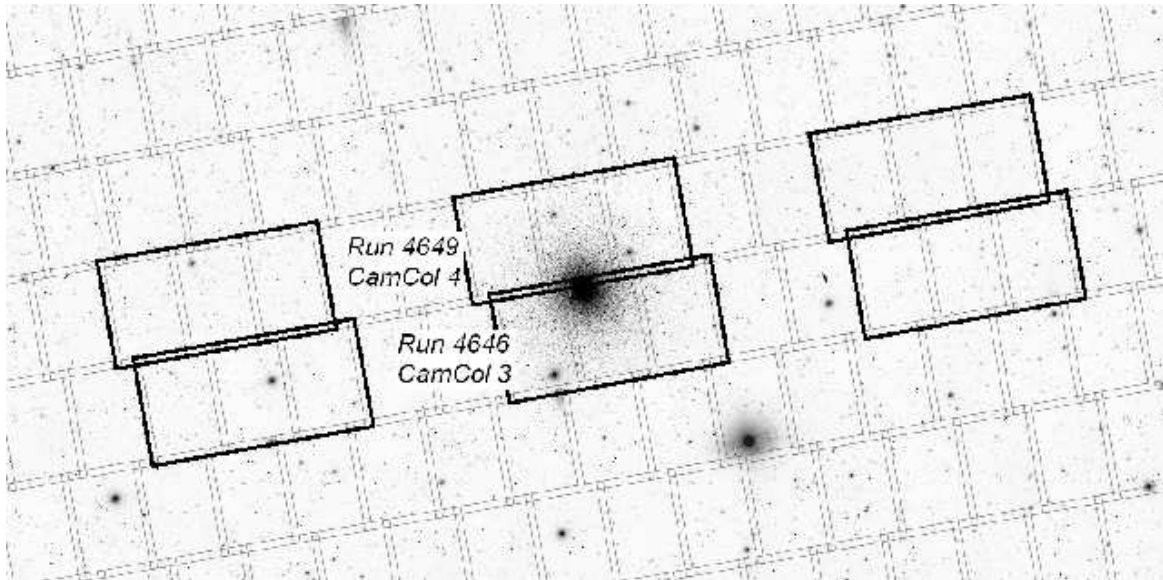


FIG. 2.— SDSS scans over the  $2^\circ \times 1^\circ$  region surrounding M3, generated using the SDSS Finding Chart Tool. Each of the horizontal strips represents a scanning footprint for each CCD. This strip is divided into rectangular frames with small overlapping regions. Adjacent strips in different runs also overlap with each other. Frames reduced in this paper are indicated as thick boxes. For each run and camcol, flanking areas are shown on each side of the cluster. North is to the top, and the east to the left.

TABLE 1  
GLOBULAR CLUSTER PROPERTIES

NGC	Alternate Name	$l$ (deg)	$b$ (deg)	$V_{\text{HB}}$ Harris	$E(B-V)$		$(m-M)_0$		[Fe/H]	
					Harris	Schlegel et al.	Harris <sup>a</sup>	Kraft & Ivans	Harris	Kraft & Ivans <sup>b</sup>
2419		180.370	+25.242	20.45	0.11	0.06	19.63	...	-2.12	...
	Pal 3	240.139	+41.861	20.51	0.04	0.04	19.84	...	-1.66	(-1.66)
	Pal 4	202.311	+71.803	20.80	0.01	0.02	20.19	...	-1.48	(-1.43)
4147		252.849	+77.189	17.01	0.02	0.03	16.42	...	-1.83	(-1.79)
5024	M53	332.967	+79.765	16.81	0.02	0.02	16.25	...	-1.99	(-2.02)
5053		335.690	+78.944	16.65	0.04	0.02	16.07	...	-2.29	(-2.41)
5272	M3	42.208	+78.708	15.68	0.01	0.01	15.09	15.02	-1.57	-1.50
5466		42.150	+73.592	16.47	0.00	0.02	16.00	...	-2.22	...
	Pal 5	0.852	+45.860	17.51	0.03	0.06	16.83	...	-1.41	...
5904	M5	3.863	+46.796	15.07	0.03	0.04	14.37	14.42	-1.27	-1.26
	Pal 14	28.747	+42.199	20.04	0.04	0.03	19.35	...	-1.52	(-1.61)
6205	M13	59.008	+40.912	15.05	0.02	0.02	14.42	14.42	-1.54	-1.60
6341	M92	68.339	+34.859	15.10	0.02	0.02	14.58	14.75	-2.28	-2.38
6838	M71	56.744	-4.564	14.48	0.25	0.32	13.02	...	-0.73	-0.81
7006		63.770	-19.407	18.80	0.05	0.08	18.09	...	-1.63	-1.48
7078	M15	65.013	-27.313	15.83	0.10	0.11	15.06	15.25	-2.26	-2.42
7089	M2	53.371	-35.770	16.05	0.06	0.04	15.30	...	-1.62	(-1.56)

<sup>a</sup> True distance modulus assuming  $A_V/E(B-V) = 3.1$  and reddening values in Harris. <sup>b</sup> [Fe/H] estimates (Kraft & Ivans 2004) in parentheses are derived from the  $[\text{Fe}/\text{H}]_{\text{II}}$  correlation with the reduced strength of the Ca II triplet (Kraft & Ivans 2003).

TABLE 2  
OPEN CLUSTER PROPERTIES

NGC	Alternate Name	$l$ (deg)	$b$ (deg)	$E(B-V)$		$(m-M)_0$	[Fe/H]	ref
				Stellar	Schlegel et al.			
2420		198.107	+19.634	0.05	0.04	12.00 <sup>a</sup>	-0.37	1
2682	M67	215.696	+31.896	0.04	0.03	9.61	+0.00	2
6791		69.958	+10.904	0.10	0.16	13.02	+0.40	3

REFERENCES. — Estimates for stellar  $E(B-V)$ ,  $(m-M)_0$ , and [Fe/H]: (1) Anthony-Twarog et al. 2006; (2) An et al. 2007b, and references therein; (3) Pinsonneault et al. 2008 (in preparation) and references therein.

<sup>a</sup> True distance modulus assuming  $A_V/E(B-V) = 3.1$ .

to derive distances to five key globular clusters from their application of the MS fitting technique. These *Hipparcos*-based distances are expected to be accurate to  $\sim 10-15\%$  (e.g., Gratton et al. 1997; Reid 1997), which will hopefully be improved greatly from upcoming astrometric missions such as *Gaia* (Perryman et al. 2001). They also provided estimates of reddening for the clusters by comparing colors derived from high-resolution spectroscopic determinations of  $T_{\text{eff}}$  with the observed colors of the same stars.

Table 2 lists reddening, distance, and metallicity estimates for our sample open clusters. For NGC 2420 we list those given by Anthony-Twarog et al. (2006), which are based on intermediate-band  $vbyCaH\beta$  photometry. For M67 we take the reddening, distance, and metallicity reported by An et al. (2007b), which is an average between literature values and those estimated using empirically calibrated sets of isochrones (see also Pinsonneault et al. 2003, 2004). The latter set of authors also used an extended set of calibrated isochrones to estimate these parameters for NGC 6791 (M. H. Pinsonneault et al. 2008, in preparation); these values are listed in Table 2. Their metallicity estimate for NGC 6791 is consistent with recent results from high-resolution spectroscopic studies (Carraro et al. 2006; Gratton et al. 2006; Origlia et al. 2006). Their reddening estimate based on the stellar sequence [ $E(B-V) = 0.10 \pm 0.01$ ] is lower than the Schlegel et al. (1998) value.

Although typical SDSS imaging scans involve small overlaps between adjacent stripes in most of the survey area, occasionally two runs from adjacent stripes overlap by a larger fraction of each field. This results in a large number of stars with repeated flux measurements, providing an opportunity to estimate realistic photometric errors (§ 4.3). Five clusters in our sample (M67, NGC 2420, NGC 5466, NGC 6791, and Pal 14) have been scanned in such a manner, covering most of the cluster fields twice.

### 3. DATA ACQUISITION AND PREPARATION

We retrieved the fpC corrected imaging frames and the fpM mask frames for the cluster fields from the Data Archive Server (DAS) for all five bandpasses. We also downloaded the best version `tsField` and `asTrans` files for each field. Table 3 lists the SDSS run, rerun, camcol, and field numbers for each cluster field analyzed. In addition to the cluster fields, we reduced flanking fields (§ 4.2) belonging to the same run, rerun, and camcol, which had considerably lower stellar densities. These fields had been successfully run through *Photo*, and are used to set the zero points for the DAOPHOT photometry by comparing the magnitudes of the stars in the two different reductions. This insures that our reductions are securely tied to the 2.5-meter *ugriz* photometric system.

Table 3 also lists the SDSS fields reduced using DAOPHOT. For cluster fields we typically combined two or three contiguous fields to form a single field, using the IRAF<sup>15</sup> package `imtile` for DAOPHOT reductions.<sup>16</sup> Some of the globular clusters subtend a small enough angle that an entire cluster fits within a single SDSS field. For these cases we did not attempt to include adjacent fields. For the flanking fields we always combined three SDSS fields to form a single field, and

<sup>15</sup> IRAF is distributed by the National Optical Astronomy Observatory, which is operated by the Association of Universities for Research in Astronomy, Inc., under cooperative agreement with the National Science Foundation.

<sup>16</sup> We use the term “field” to represent the combined SDSS fields, each of which is defined as the data processing unit in *Photo*.

TABLE 3  
FRAMES REDUCED

Cluster Name	Run-ReRun-CamCol	Fields	
		Cluster	Flanking
NGC 2420	2888-40-3	024-026	020-022/028-030
	3462-40-6	024-026	019-021/028-030
	3513-40-6	021-023	016-018/025-027
NGC 2419	1350-40-4	054	049-051/057-059
	1402-40-6	044-046	040-042/048-050
M67	5935-40-2	108-110	103-105/112-114
	5972-40-6	117-119	112-114/121-123
	6004-40-5	114-116	109-111/118-120
Pal 3	2141-40-4	059	054-056/062-064
Pal 4	5061-40-3	375	370-372/378-380
	5071-40-2	373	368-370/376-378
NGC 4147	5360-40-6	239	234-236/243-245
	5381-40-6	186	181-183/189-191
M53	5360-40-6	338-340	333-335/343-345
	5390-40-6	161-163	156-158/166-168
NGC 5053	5360-40-5	344-345	339-341/348-350
	5390-40-5	167-168	162-164/171-173
M3	4646-40-3	080-082	075-077/085-087
	4649-40-4	145-147	140-142/150-152
NGC 5466	4623-40-1	324-325	319-321/327-329
	4646-40-6	114-115	109-111/118-120
Pal 5	0756-44-3	755-757	751-753/760-762
M5	1458-40-4	699-701	694-696/704-706
	2327-40-4	048-049	043-045/052-054
Pal 14	4670-40-2	302	297-299/305-307
	5323-40-6	095	090-092/098-100
M13	3225-40-4	264-266	259-261/268-270
	3226-40-5	126-128	121-123/131-133
M92	4682-40-6	207-209	202-204/211-213
	5327-40-6	013-014	017-019
NGC 6791	5403-40-4	190-192	185-187/195-197
	5416-40-3	190-192	186-188/194-196
	6177-40-3	043-045	039-041/047-049
M71	6895-40-3	052-053	056-058
NGC 7006	4879-40-2	091	086-088/094-096
	M2	2583-40-2	135-137
M15	2662-40-1	037-038	032-034/041-043
	1739-40-6	058-059	053-055/062-064
	2566-40-6	064-065	059-061/068-070

reduced it as a single data processing unit in DAOPHOT.

Before running DAOPHOT, we removed the softbias of 1000 DN and masked pixels affected by saturation. DAOPHOT identifies pixels above a “high good datum” value as saturated. However, for SDSS a saturated pixel will overflow and pour charge into its neighbors. This results in distorted shapes for the PSF of the brightest stars, but without necessarily setting the counts in an affected pixel above a certain value. It is also noted that the full well depth varies from chip to chip. To set the pixel value to a large number, we used the SDSS `readAtlasImages` code<sup>17</sup> to set the pixels flagged as saturated, as well as the pixels within a radius of 3 pixels, equal to 70000 DN. The bad pixel value in DAOPHOT was then set to 65000 DN. The gain and readnoise values for each chip and filter are listed in Table 4.

## 4. CROWDED FIELD PHOTOMETRY

### 4.1. DAOPHOT/ALLFRAME Reduction

The goal of this study is to obtain accurate photometry for stars in the crowded cluster fields using the same final aperture radius as the SDSS data, which is 18.584 pixels (7.43’). We used DAOPHOT and its accompanying program ALLSTAR to find stars, derive a spatially varying PSF, and perform the

<sup>17</sup> [www.sdss.org/dr6/products/images/read\\_mask.html](http://www.sdss.org/dr6/products/images/read_mask.html)

TABLE 4  
 DETECTOR PROPERTIES

CamCol	GAIN (e <sup>-</sup> /DN)					READ NOISE (DN <sup>2</sup> )				
	<i>u</i>	<i>g</i>	<i>r</i>	<i>i</i>	<i>z</i>	<i>u</i>	<i>g</i>	<i>r</i>	<i>i</i>	<i>z</i>
1	1.62	3.32	4.71	5.17	4.75	9.61	15.60	1.82	7.84	0.81
2	1.60	3.86	4.60	6.57	5.16	12.60	1.44	1.00	5.76	1.00
3	1.59	3.85	4.72	4.86	4.89	8.70	1.32	1.32	4.62	1.00
4	1.60	4.00	4.76	4.89	4.78	12.60	1.96	1.32	6.25	9.61
5	1.47	4.05	4.73	4.64	3.48	9.30	1.10	0.81	7.84	1.82
6	2.17	4.04	4.90	4.76	4.69	7.02	1.82	0.90	5.06	1.21

first measurements for all stars in a single field and a single filter. We then matched the stars from all the filters in a single field, using DAOMATCH and DAOMASTER, to form a master list that served as the input into ALLFRAME, which simultaneously reduces all the data for a particular field. The remainder of this section describes the reduction process in detail.

Stars were identified in each frame using DAOPHOT/FIND, with a threshold of  $4\sigma$ , a low sharpness<sup>18</sup> cutoff of 0.30, a high sharpness cutoff of 1.40, a low roundness cutoff of  $-1.00$ , and a high roundness cutoff of 1.00. The FWHM parameter, which is used to define the Gaussian that detects stars, was set to the average FWHM of stars in each frame. Since our goal is to derive cluster fiducial sequences rather than cluster luminosity functions, no effort was made to correct for incompleteness, which obviously increases in the more crowded regions.

For each frame, a large number ( $\sim 100-300$ ) of relatively isolated stars spread across the frame were chosen as PSF stars. The fitting radius of the PSF in the  $\chi^2$  minimization was set to 5 pixels. The PSF was calculated out to a radius of 15 pixels, which defines how far out the light from the star was subtracted on the image. DAOPHOT first determined a constant, analytic PSF across the entire field. Neighboring stars of the PSF stars were identified. Next, the neighboring stars were subtracted using ALLSTAR with the first pass PSF. The PSF was then re-determined with both the analytic and look-up table components. This new PSF was then used to subtract the neighbors. The next iteration allowed the PSF to vary linearly across the frame, and subsequent iterations increased the variability to quadratic and finally cubic. ALLSTAR was then run on the entire field. The subtracted image was searched for additional stars, this time with a threshold of  $10\sigma$ , before the final ALLSTAR run was performed on all stars.

Before we can run ALLFRAME, we need to provide a master list of stars so that the same stars can be used to reduce each frame. In contrast to the usual method of crowded field photometry, where multiple long and short exposures are taken in all filters, SDSS scans most regions once, with only small parts of the frames overlapping with a separate scan. Therefore, the standard technique of using exposures in the same filter to eliminate cosmic rays and spurious detections (e.g., in the bright wings of badly subtracted stars) is not possible.

Instead, we relied on multiple detections in different filter bandpasses to reduce the chances of spurious detections. We first used DAOMATCH and DAOMASTER to match stars among different filter frames. We then made a master star

list, requiring that a star should appear in at least two of the frames. This leads to the possibility that a star could be a real detection in one of the bandpasses, but be eliminated because of a lack of detection in the other four filters. However, our selection criterion, with a minimum two detections in different filter frames, insures that each star has at least one color, which is crucial in the derivation of the fiducial sequences. The master list served as the input for ALLFRAME, which simultaneously determines the separate brightnesses for stars in all frames while enforcing one set of centroids and one transformation between images.

Finally, we applied aperture corrections to obtain the instrumental magnitude of a star within an 18.584 pixel aperture radius. After subtracting all other stars, we measured the aperture magnitudes for the PSF stars through 12 different radii. We used HSTDAOGROW, which is a modified version of DAOGROW (Stetson 1990), to calculate the total magnitude by the curve of growth method. The difference between these programs is that HSTDAOGROW does not extrapolate to twice the largest aperture, as is done by DAOGROW. The difference between the PSF magnitude and the aperture magnitude for each star defines the aperture correction. We calculated the average difference after iterating twice and discarding stars that were more than 1.8 times the rms away from the mean. This final average aperture correction was applied to all of the PSF magnitudes.

We converted (aperture-corrected PSF) DAOPHOT (Pogson) magnitudes into the SDSS asinh magnitude system (luptitude; Lupton et al. 1999) using the photometric zero point (aa), extinction coefficient (kk), and air-mass (airmass) values from the `tsField` files:

$$\text{mag} = -(2.5/\ln(10))[asinh((f/f_0)/2b) + \ln(b)] \quad (1)$$

where  $b$  is the softening parameter for the photometric band in question<sup>19</sup> and

$$f/f_0 = (\text{counts}/53.907456 \text{ sec}) \times 10^{0.4(\text{aa} + \text{kk} \times \text{airmass})}. \quad (2)$$

The air-mass value used was either the one for the central frame, if three frames were used, or the eastern frame of the cluster field set. Any changes in air mass during the time of the 2-3 frame scan were negligible.

We used `cvcoords` in the SDSS astrotols suite of programs as well as the information in the `astrans` files from the DAS to determine celestial coordinates of right ascension and declination of the stars in the *r*-band images. Astrometric positions in SDSS are accurate to  $< 0.1''$  for sources with  $r < 20.5$  mag (Pier et al. 2003).

<sup>18</sup> The index sharpness in DAOPHOT/FIND is defined as the ratio of the height of the bivariate delta-function, which best fits the brightness peak, to the height of the bivariate Gaussian function, which best fits the peak.

<sup>19</sup> The following softening parameter  $b$  values are used in SDSS:  $1.4 \times 10^{-10}$ ,  $0.9 \times 10^{-10}$ ,  $1.2 \times 10^{-10}$ ,  $1.8 \times 10^{-10}$ , and  $7.4 \times 10^{-10}$  in *u*, *g*, *r*, *i*, and *z*, respectively. See also <http://www.sdss.org/dr6/algorithms/fluxcal.html>.

#### 4.2. Photometric Zero Points

Our initial DAOPHOT reductions in relatively low stellar-density fields showed that there exist  $\sim 0.02$  mag differences between DAOPHOT and *Photo* magnitudes. Since the DAOPHOT reduction in this study does not include photometric standard fields to independently calibrate the data, we put the DAOPHOT magnitudes onto the *Photo* scale as described below.

##### 4.2.1. Data

In order to place our DAOPHOT photometry on the same scale as that determined by *Photo*, it was necessary to compare results for stars that are far enough from the clusters' dense stellar fields to avoid crowding effects, but close enough to represent the local photometric properties near the clusters. These comparisons are accomplished by using stars contained in a set of flanking fields that lie at least two frames away ( $\approx 20'$ ) from the crowded cluster fields. An example of flanking fields is shown in Figure 2 for M3.

The location of these flanking fields is largely based on how *Photo* computes the model PSF. In *Photo*, the PSF is modeled using a Karhunen-Loève (KL) transform, where stars lying in  $\pm 2$  adjacent frames (in the scan direction) are used to determine the KL basis functions (Lupton et al. 2002). At the same time, *Photo* also relies upon stars in  $\pm 0.5$  adjacent frames to follow the spatial (temporal) variation of the PSF. Therefore, the two closest fields to a cluster, where *Photo* has modeled the PSF without using stars in the crowded region, are those that are two frames away from the crowded fields.

For each run and camcol we selected flanking areas on each side of a cluster, which we refer to as western and eastern flanking fields. We combined three contiguous fields to form a single flanking field and derived stellar magnitudes following the same procedure as cluster photometry using DAOPHOT. By analyzing three combined fields instead of just one, we had a larger number of bright PSF stars, especially in relative sparse halo fields. We typically selected 50–100 PSF stars in each flanking field with good signal-to-noise ratios ( $r \lesssim 18$  mag), and used a model PSF that varies cubically with position. Although we had only  $\sim 30$  PSF stars in the *u*-band frames for about one third of our flanking fields, we found that the cubically varying PSF is necessary to adequately reduce data in these fields. We used HSTDAOGRROW to determine aperture corrections, and converted DAOPHOT magnitudes into the SDSS asinh magnitudes.

To derive an accurate photometric zero point, we used photometry with errors smaller than 0.05 mag in each band (errors reported from DAOPHOT) for stars brighter than 15.5 mag in *u*, 16.0 mag in *gri*, and 15.0 mag in *z*. We additionally filtered data based on the sharp<sup>20</sup> and  $\chi$  values from DAOPHOT. We adopted  $|\text{sharp}| < 1$  and  $\chi < 1.5 + 4.5 \times 10^{-0.4(m-m_0)}$  (Stetson et al. 2003), where  $m_0 = 15.5$  mag in *u*,  $m_0 = 16.0$  mag in *gri*, and  $m_0 = 15.0$  mag in *z*, in order to remove objects that have relatively poor goodness-of-fit values.

We retrieved *Photo* PSF magnitudes either from the Catalog Archive Server (CAS) in the Sixth Data Release, or directly from the `tsObject` files when the data were not yet available through the data release. We used *Photo* magnitudes for stars that passed a set of photometric criteria to obtain

clean photometry. We selected objects that are classified as STAR (unresolved point sources) and used SDSS primary or secondary detections with photometric errors smaller than 0.05 mag. For the *r*-band image of run 5071, camcol 2, field 376 (hereafter we use the format 5071-r2-376 to represent a specific frame) and 6895-i3-56, we relaxed the threshold to 0.06 mag because all of the *Photo* magnitudes in these fields have errors larger than 0.05 mag. We ignored photometry for objects that have the following flags set: `EDGE`, `NOPROFILE`, `PEAKCENTER`, `NOTCHECKED`, `PSF_FLUX_INTERP`, `SATURATED`, `BAD_COUNTS_ERROR`, `DEBLEND_NOPEAK`, `INTERP_CENTER`, or `COSMIC_RAY` (e.g., Ivezić et al. 2007).<sup>21</sup> We employed these selection criteria in each filter bandpass, in order not to eliminate a star from all of the filter frames even if it was flagged or had a large error in one of the bandpasses. This helps to keep many of the point sources that were poorly detected in the *u*-band frames. We then cross-matched photometry in *Photo* and DAOPHOT, using a search radius of 3 pixels.

##### 4.2.2. Comparison with Photo

For the flanking fields we first compared the number of stellar objects found by DAOPHOT and *Photo*. In the *r* band, DAOPHOT detected  $\sim 50$  to  $\sim 5000$  stellar sources on each (SDSS) field with  $r < 20$  mag. Among these, *Photo* recovered on average  $75\% \pm 9\%$  of the sources classified as STAR, except in the case of M71 flanking field 6895-r3-56/57/58 (see below). All detections in *Photo* were recovered by DAOPHOT; there is no apparent trend of the detection rate in *Photo* as a function of the total number of detected sources in DAOPHOT. The average recovery fraction in *Photo* becomes  $87\% \pm 4\%$  when we matched sources in DAOPHOT with the above  $\chi$  and sharp index selections.

Figure 3 shows the comparison between DAOPHOT and *Photo* magnitudes in one of the flanking fields for M13, 3226-5-121/122/123. The constant offsets between the two are the zero-point corrections that will be applied to the cluster photometry. However, we noted that there are systematic variations in the difference, at a level of  $\sim 2\%$ , in the scan direction or over time, in addition to photon noise. These high spatial frequency structures are likely due to fast PSF variations, which were not followed by the PSF of *Photo* on a rapid enough spatial or temporal scale.

The accuracy of PSF photometry can be best tested from the comparison with aperture photometry for isolated bright stars. Specifically, we can use the individual aperture corrections to test how accurately our model PSF accounted for the variability of the PSF by plotting the difference between the PSF magnitude and the aperture magnitude as a function of position. If we have modeled the variability of the PSF sufficiently well, there will be no dependence of that difference on the position of the stars on the chip.

Figure 4 shows the differences between the DAOPHOT PSF and aperture magnitudes, with aperture radii of 18.584 pixels from the HSTDAOGRROW analysis. Individual points are those used in our PSF modeling, and an average offset in each panel represents the aperture correction for DAOPHOT PSF photometry in each filter bandpass. The same fields are shown as in the above comparison with *Photo*. However, in contrast to the systematic variations seen in Figure 3, the differences

<sup>20</sup> The index sharp used here is defined differently from the sharpness index in DAOPHOT/FIND:  $\text{sharp}^2 \approx |s_{\text{obs}}^2 - s_{\text{PSF}}^2|$  where  $s_{\text{obs}}$  is a characteristic radius of the measured image profile, and  $s_{\text{PSF}}$  is a characteristic radius of the PSF. The sign of the sharp index is positive if  $s_{\text{obs}} > s_{\text{PSF}}$ .

<sup>21</sup> See also <http://www.sdss.org/dr6/products/catalogs/flags.html>.

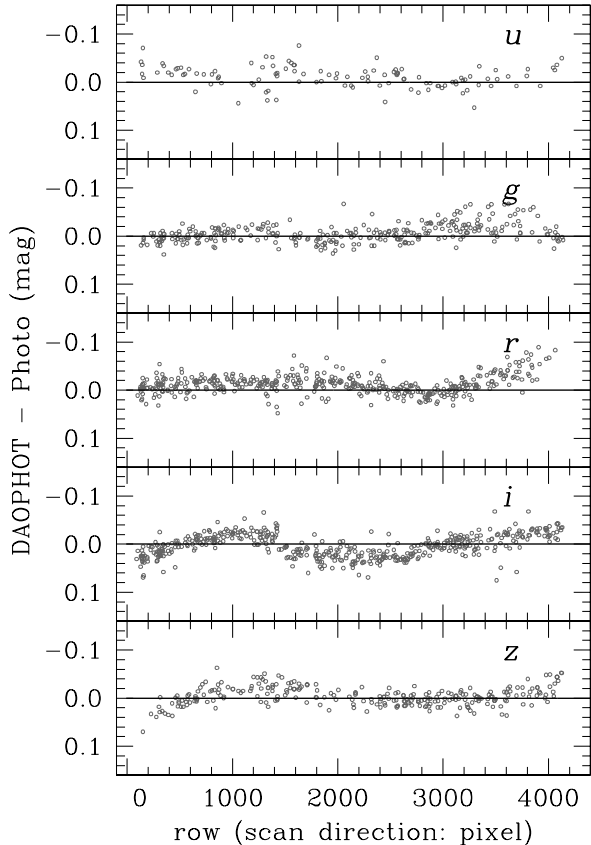


FIG. 3.— Comparison between the DAOPHOT and the *Photo* magnitudes in one of the M13 flanking fields. Comparisons are shown for *u*, *g*, *r*, *i*, and *z*, from the top to the bottom panels.

between the DAOPHOT and aperture magnitudes are quite uniform, to better than 1% accuracy, over a time scale covered by at least one flanking field ( $\sim 30'$  or  $\sim 3$  min in time). This test shows that the systematic residuals in Figure 3 are due to errors in the *Photo* magnitudes, presumably due to imperfect modeling of the PSFs. In support of this conclusion, we found similar high spatial frequency structures (in size and amplitude) as those in Figure 3, obtained from the comparison between the *Photo* PSF and aperture 7 magnitudes (flux measurements with an 18.584 pixel aperture from *Photo*).

Other flanking fields also exhibit stable differences between DAOPHOT magnitudes and aperture photometry, but exhibit systematic variations of *Photo* magnitudes, seen most clearly in the scanning direction. After iterative  $3\sigma$  clipping, we computed a rms dispersion for each field and estimated a median of the rms from all of our flanking fields (except for the few cases discussed below). From a comparison between the HST-DAOGROW aperture magnitudes and the DAOPHOT magnitudes, we found a median rms of 0.0061 mag, 0.0039 mag, 0.0045 mag, 0.0052 mag, and 0.0054 mag in *ugriz*, respectively, yielding a precise aperture correction and its spatial uniformity. From the comparison between *Photo* and DAOPHOT, however, we found a factor of three larger rms values: 0.0198 mag, 0.0172 mag, 0.0162 mag, 0.0176 mag, and 0.0173 mag in *ugriz*, respectively (Fig. 5). We note that Smolčić et al. (2007) compared the DoPHOT and *Photo* photometry in an uncrowded field and estimated the rms differences of 0.029 mag, 0.013 mag, 0.027 mag in *gri*, respectively.

The 2% variation of *Photo* is consistent with the spec-

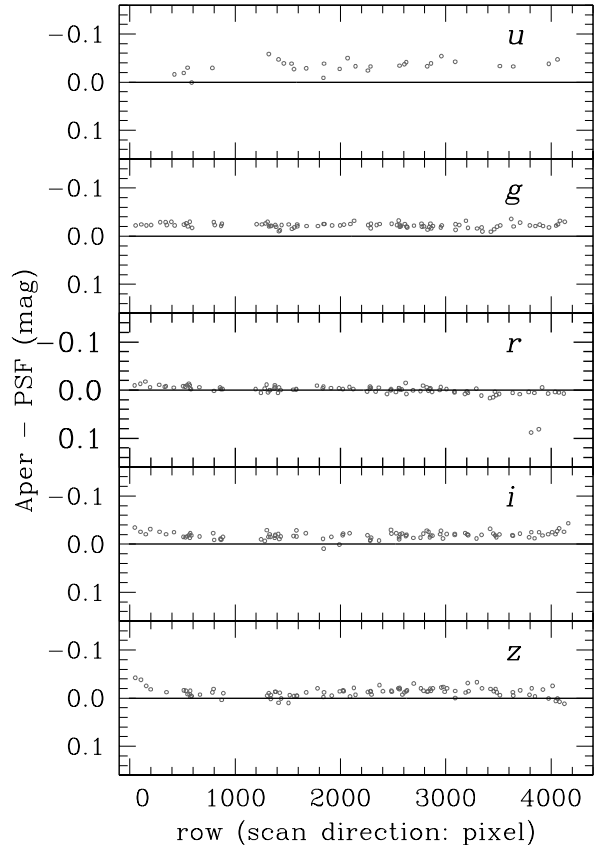


FIG. 4.— Comparison between the DAOPHOT and the aperture photometry in the same flanking field as in Fig. 3. The aperture photometry was derived using HSTDAOGROW for PSF stars, shown as circles. Comparisons are shown for *u*, *g*, *r*, *i*, and *z*, from the top to the bottom panels.

ified size of the photometric errors in the SDSS project (Ivezić et al. 2003, 2004). While this level of accuracy already makes SDSS one of the most successful optical surveys (see also Sesar et al. 2006), the spatial variations of the *Photo* PSF magnitudes clearly indicates that there is room for future improvement in the photometric accuracy (e.g., Ivezić et al. 2007; Padmanabhan et al. 2008).

There is a small fraction of cases where DAOPHOT magnitudes vary significantly with respect to aperture photometry over a given frame. In some of these cases the difference between the DAOPHOT and the aperture photometry jumps by  $\sim 0.02$  mag systematically in some parts of the flanking fields. These abrupt variations are strongly correlated with the change in the PSF shapes, which may be caused by a sudden change in the telescope focus or tracking.

We initially attempted to model these spatially varying PSFs by reducing individual frames of each flanking field. However, we found that, in most cases, the sudden PSF variations could not be adequately modeled by cubically varying the PSFs in DAOPHOT, so we decided not to include such fields in the following analyses. The problematic flanking fields have significantly large rms values in the comparison with aperture photometry, so we used rms cuts of 0.040 mag in the *u* band and 0.020 mag in *griz*, after initial  $5\sigma$  clipping, to identify them. A total of nine flanking fields (2% of all of the 380 flanking fields in this study) were rejected using these cuts: 3462-r6-19/20/21, 4649-i4-150/151/152, 5071-u2-368/369/370,

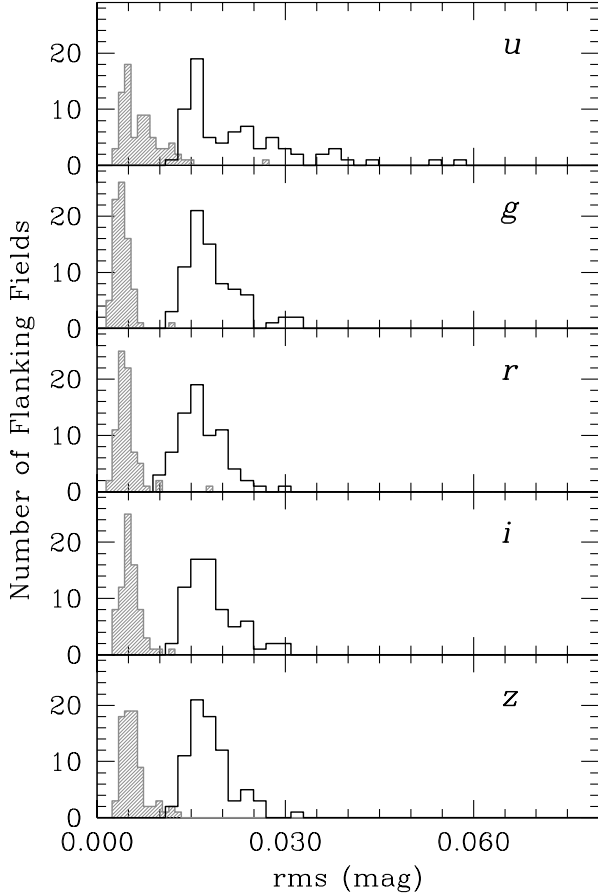


FIG. 5.— Distribution of the rms differences between the DAOPHOT and the aperture photometry (grey shaded histogram) and between the DAOPHOT and the *Photo* photometry (black histogram) from all of the flanking fields.

5071-i2-368/369/370,  
 5360-u5-339/340/341,  
 5360-i5-339/340/341,  
 5360-r6-343/344/345,  
 6004-r5-109/110/111, 6004-i5-109/110/111.  
 For these runs we used photometry in a flanking field on the other side of a cluster to set the photometric zero points.

Among the fields with small rms differences between the aperture and the DAOPHOT photometry, the DAOPHOT magnitudes show particularly large rms differences with *Photo* ( $> 0.050$  mag after initial  $5\sigma$  clipping) in two flanking fields: 5403-r4-185/186/187 (NGC 6791 run) and 6895-i3-56/57/58 (M71 run). In the former case, most of the dispersion comes from a strong discontinuity in the magnitude difference of the field 187, when compared with the preceding two fields. In the last field, the PSP\_FIELD\_PSF11 flag in PspStatus was set, indicating that *Photo* magnitudes were derived using a spatially (temporally) constant PSF. We did not use this field in the following analyses.

The 6895-3-56/57/58 (M71 run) has the highest stellar density among cluster flanking fields in this study. Approximately 15000 point sources were found in one flanking field with  $r < 20$  mag from DAOPHOT. The large rms observed in this field was caused by a magnitude-dependent trend in the difference between DAOPHOT and *Photo* (which is not seen in other flanking fields): *Photo* detections become

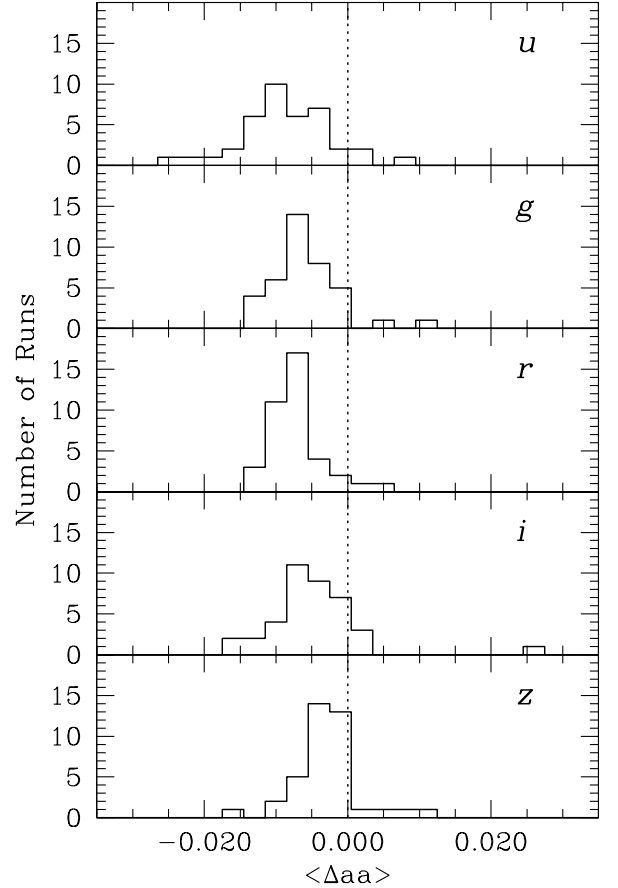


FIG. 6.— Distribution of the zero-point corrections for the DAOPHOT photometry.

fainter with increasing apparent magnitude. One likely explanation is that *Photo* over-estimates the sky brightness in crowded fields, where it fails in the detection and subtraction of faint objects. In fact, *Photo* detected only  $\sim 700$  sources classified as STAR with  $r < 20$  mag in this flanking field and does not report flux measurements in the other flanking field. We derived zero-point differences between *Photo* and DAOPHOT using bright stars with  $u < 20$  mag,  $g < 19$  mag,  $r < 18$  mag,  $i < 18$  mag, and  $z < 17$  mag.

For each flanking field we took an average over three fields to determine a zero-point correction,  $\Delta aa$ , for DAOPHOT:

$$\Delta aa \equiv aa^{\text{DAOPHOT}} - aa^{\text{Photo}} = \langle m_i^{\text{DAOPHOT}} - m_i^{\text{Photo}} \rangle. \quad (3)$$

We then averaged results from two flanking fields on each run, filter, and camcol, with weights given by the errors in  $\Delta aa$ . These are either the propagated error from the *Photo* comparison on each flanking field, or the difference in  $\Delta aa$  between western and eastern flanking fields divided by two, whichever is larger. Table 5 lists new aa coefficients for our fields. The second and third columns in Table 6 list the average zero-point correction and rms dispersion in each bandpass, respectively, from all of our flanking fields. As also shown in Figure 6, the  $u$  band has the largest average correction among bandpasses, with  $\langle \Delta aa \rangle \approx -0.009$ , while longer wavelength filters have smaller  $\langle \Delta aa \rangle$  values. These zero-point corrections are systematic in nature and statistically significant.

The cause of the zero-point difference remains unclear. It could be an error in the aperture correction, or it could be due to different ways of determining sky values in the two

TABLE 5  
THE aa COEFFICIENTS FOR DAOPHOT

Run	CamCol	aa_u	aa_g	aa_r	aa_i	aa_z	Cluster
756	3	-24.1047	-24.5849	-24.1775	-23.7702	-21.8598	Pal5
1350	4	-24.0218	-24.5221	-24.0788	-23.7370	-21.8173	NGC2419
1402	3	-24.0123	-24.4928	-24.0966	-23.7079	-21.8016	NGC2419
1458	4	-23.9525	-24.4824	-24.0408	-23.6922	-21.7321	M5
1739	6	-23.5430	-24.3924	-24.0260	-23.6522	-21.8577	M15
2141	4	-23.9682	-24.4864	-24.0662	-23.7309	-21.8065	Pal3
2327	4	-23.8256	-24.4737	-24.0553	-23.7266	-21.8064	M5
2566	6	-23.4285	-24.3798	-23.9759	-23.6428	-21.8381	M15
2583	2	-23.7293	-24.3516	-23.9822	-23.5582	-21.8425	M2
2662	1	-23.9651	-24.5883	-24.0796	-23.6851	-22.0001	M2
2888	3	-23.8460	-24.4556	-24.0773	-23.7461	-21.8830	NGC2420
3225	4	-23.7044	-24.4065	-23.9744	-23.6809	-21.7117	M13
3226	5	-23.9337	-24.3186	-24.0345	-23.6193	-22.2724	M13
3462	6	-23.5143	-24.4859	-24.0565	-23.6935	-21.9792	NGC2420
3513	6	-23.5261	-24.4528	-24.0475	-23.6957	-21.9535	NGC2420
4623	1	-23.8607	-24.5685	-24.0320	-23.6199	-21.9555	NGC5466
4646	3	-23.7777	-24.4222	-23.9935	-23.6680	-21.7882	M3
4646	6	-23.4123	-24.3961	-23.9683	-23.6237	-21.9051	NGC5466
4649	4	-23.7366	-24.4195	-23.9497	-23.6788	-21.7534	M3
4670	2	-23.7051	-24.4017	-23.9825	-23.5853	-21.9417	Pal14
4682	6	-23.4981	-24.4152	-23.9959	-23.6507	-21.9315	M92
4879	2	-23.7270	-24.4404	-24.0645	-23.6569	-21.9531	NGC7006
5061	3	-23.8128	-24.4389	-24.0376	-23.7196	-21.8324	Pal4
5071	2	-23.7610	-24.4030	-24.0285	-23.6435	-22.0033	Pal4
5323	6	-23.3916	-24.4289	-24.0283	-23.6781	-21.9806	Pal14
5327	6	-23.4375	-24.4386	-24.0427	-23.6906	-21.9649	M92
5360	5	-23.9117	-24.3206	-24.0069	-23.6301	-22.3503	NGC5053
5360	6	-23.3901	-24.3960	-23.9773	-23.6301	-21.9294	NGC4147
5360	6	-23.3998	-24.4025	-23.9855	-23.6411	-21.9304	M53
5381	6	-23.3332	-24.4052	-23.9971	-23.6417	-21.9385	NGC4147
5390	5	-23.8879	-24.3443	-24.0286	-23.6446	-22.3340	NGC5053
5390	6	-23.3636	-24.4049	-23.9863	-23.6236	-21.8995	M53
5403	4	-23.6659	-24.4256	-23.9299	-23.7138	-21.7897	NGC6791
5416	3	-23.7120	-24.3963	-24.0259	-23.6750	-21.8010	NGC6791
5935	2	-23.6510	-24.3622	-23.9817	-23.5872	-21.9635	M67
5972	6	-23.3384	-24.3808	-23.9791	-23.6422	-21.9654	M67
6004	5	-23.8660	-24.3285	-24.0502	-23.6612	-22.3708	M67
6177	3	-23.9108	-24.4583	-24.0660	-23.7181	-21.8399	NGC6791
6895	3	-23.7923	-24.4366	-24.0421	-23.6497	-21.7717	M71

TABLE 6  
STATISTICAL PROPERTIES OF ZERO-POINT CORRECTIONS IN  
FLANKING FIELDS

Filter	$\langle \Delta aa \rangle$		$N_{\text{run}}$	$\Delta aa^{\text{west}} - \Delta aa^{\text{east}}$		$N_{\text{run}}^a$
	average	rms		average	rms	
<i>u</i>	-0.0092	0.0063	39	+0.0023	0.0082	35
<i>g</i>	-0.0062	0.0046	39	+0.0019	0.0060	37
<i>r</i>	-0.0068	0.0040	39	-0.0004	0.0074	33
<i>i</i>	-0.0053	0.0069	39	+0.0025	0.0052	33
<i>z</i>	-0.0034	0.0044	39	-0.0003	0.0057	37

<sup>a</sup> The total number of comparisons in this column is smaller than the total number of runs in this study ( $N_{\text{run}} = 39$ ) because some of the runs have only one flanking field available in the analysis.

data reduction procedures. To scrutinize this issues, one may wish to reduce secondary patches using DAOPHOT and independently calibrate DAOPHOT magnitudes. However, this requires a significant amount of data reduction with human intervention (e.g., PSF selection). Therefore, we chose to put DAOPHOT photometry onto the *Photo* system, which is internally defined in a self-consistent manner, and avoid any discussion of the absolute calibration in this paper. The new zero points ( $aa^{\text{DAOPHOT}}$ ) derived from the *Photo* comparisons were used, along with the extinction coefficient (*kk*) and airmass (*airmass*) values, to derive magnitudes for stars in the crowded cluster fields (Eqs. 1 and 2).

### 4.3. Photometric Errors

To assess the accuracy of our photometry, we need to know both how well we can determine the zero point of the calibration and how well we can measure the brightness of a particular star, which can be affected by the degree of crowding as well as by photon noise. We first consider zero-point errors, followed by a discussion of the random star-by-star errors.

#### 4.3.1. Zero-Point Accuracy

Systematic zero-point errors for the DAOPHOT photometry are the results of uncertainties in the aperture correction, the derivation of zero-point differences between DAOPHOT and *Photo* magnitudes, and the intrinsic zero-point errors in the reference *Photo* system. The zero-point errors in *Photo* can be further divided into an absolute calibration error, which can be reduced to a problem of tying the SDSS magnitude system to an AB system (Abazajian et al. 2004), and a relative zero-point calibration error. The latter is exhibited as spatial variations in the calibration on the sky, or differences in flux measurements for stars observed in overlapping runs.

To assess the zero-point errors we took the following two approaches. Firstly, we compared the DAOPHOT photometry in flanking fields to the *Photo* values, in order to check the spatial stability of the *Photo* zero points over several frames. We took into account the fact that all of the above error components, except the absolute calibration error, will manifest

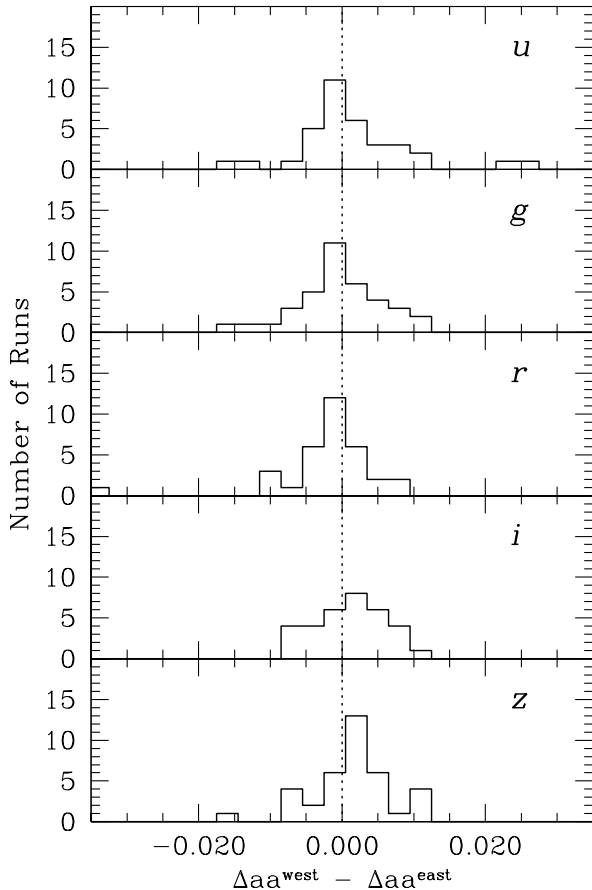


FIG. 7.— Distribution of zero-point differences between the western and the eastern flanking fields.

themselves collectively as differences in the *Photo* comparisons. Secondly, we used multiple measurements for sources detected in more than two different runs to assess the zero-point errors. A discussion on absolute calibration errors is beyond the scope of this paper.

In § 4.2 we showed that the DAOPHOT PSF magnitudes are spatially and temporally uniform to  $\sim 0.005$  mag with respect to the aperture photometry. Given this high internal precision of the photometry,  $\sim 2\%$  spatial (temporal) variations in the difference between the DAOPHOT and the *Photo* magnitudes on a sub-field scale (e.g., Fig. 3) were attributed to the PSF modeling errors in *Photo*. Nevertheless, these high spatial frequency structures are not a significant error component of the DAOPHOT zero point because we took an average of the difference between the two photometric measurements with a large number of comparison stars in each flanking field ( $< 0.001$  mag).

We investigated an additional error component of the photometric zero point by comparing results from the western and eastern flanking fields. The two flanking fields on each run and camcol are separated by about 10 fields. Therefore, a zero-point variation over a large angular scale ( $\sim 1.5^\circ$  or  $\sim 10$  min in scanning time), or the difference in zero-point corrections in these two fields ( $\Delta aa^{\text{west}}$  and  $\Delta aa^{\text{east}}$  for the western and eastern fields, respectively) can be used as a measure of the zero-point shifts.

Figure 7 shows the distribution of zero-point differences in the western and eastern fields for all pairs of the flank-

ing fields. The fifth column in Table 6 lists the global average of the zero-point difference, which is generally consistent with zero in all of the filter bandpasses. However, zero points from the western and eastern flanking fields typically differ by  $\sim 0.006$  mag on each run, as shown in the sixth column. This indicates that DAOPHOT magnitudes will have a mild zero-point variation over an  $\sim 1.5^\circ$  scale, which is smaller than the  $\sim 0.02$  mag fluctuations seen on a sub-field scale.

However, it should be kept in mind that the above comparisons are based on flux measurements in each run and camcol, which have the same *aa* and *kk* coefficients from the *tsField* files. As a second approach, we assessed the zero-point errors by comparing flux measurements from overlapping regions between different strips and runs. A small fraction of stars are found in overlapping strips, and their fluxes were individually measured and calibrated to the *Photo* system for each run in the DAOPHOT reduction. Therefore, the net magnitude difference between the two runs directly measures the reliability of our photometric zero points.

Table 7 shows comparisons for the DAOPHOT magnitudes from all of the overlapping runs. The second and third column list two runs in the comparison. A “reference” run was selected if it covers a larger fraction of a cluster than a “comparison” run, otherwise a small-numbered run was chosen. In the derivation of the fiducial sequences (§ 5.2) we use the local zero point set by the reference runs to combine photometry from two different runs. The fourth through eighth columns list weighted average magnitude differences in the five passbands. We matched stars from separate runs using the celestial coordinates with a match radius of  $1''$ . We used stars that satisfy the same selection criteria on magnitudes, errors,  $\chi$ , and sharp index values as in § 4.2. However, in the *u*-band and *z*-band frames, we relaxed the thresholds on magnitude errors to 0.10 mag to include more comparison stars in these small overlapping regions. We further increased the threshold for the *u*-band matches to 0.30 mag in some clusters (M53, M92, NGC 4147, NGC 5053, and Pal 14), which have an even smaller number of comparison stars. For Pal 4 we did not compute the zero-point difference in the *u* band because no stars were found in that filter frame that satisfy our  $\chi$  and sharp index criteria.

The rms of these differences from all comparisons are 0.042 mag, 0.021 mag, 0.027 mag, 0.024 mag, and 0.026 mag in *ugriz*, respectively. In Table 7 we also found that the rms differences in colors are 0.040 mag in *u-g*, 0.021 mag in *g-r*, 0.017 mag in *g-i*, and 0.021 mag in *g-z*. Although there is a mild zero-point variation over  $\sim 10$  fields ( $\sim 0.6\%$ ), the calibration accuracy of the DAOPHOT photometry is predominantly limited by these  $\sim 2\%$  run-to-run zero-point variations. Our results are consistent with a zero-point uncertainty of  $\sim 2\%–3\%$  in *Photo* (Ivezić et al. 2004).

#### 4.3.2. Random Errors

Repeated flux measurements in overlapping strips/runs also provide an opportunity to determine the star-to-star uncertainties in the photometry. We used the same matched list of stars as in the previous section, but without the cuts on magnitudes and magnitude errors. We adjusted the net zero-point differences between the runs (Table 7) before making the photometric comparisons and then estimated the standard deviations of individual measurements. We only considered double measurements, although some of the stars in the open cluster fields have been detected in three runs.

Figure 8 shows the standard deviations of individual mea-

TABLE 7  
PHOTOMETRIC COMPARISONS IN OVERLAPPING RUNS

Cluster	Runs		Ref. - Comp. (mag)				
	Ref.	Comp.	$\langle\Delta u\rangle$	$\langle\Delta g\rangle$	$\langle\Delta r\rangle$	$\langle\Delta i\rangle$	$\langle\Delta z\rangle$
M2	2583	2662	$+0.051 \pm 0.005$	$-0.016 \pm 0.001$	$+0.005 \pm 0.002$	$+0.002 \pm 0.002$	$+0.027 \pm 0.002$
M3	4646	4649	$-0.041 \pm 0.006$	$-0.018 \pm 0.002$	$-0.044 \pm 0.001$	$-0.033 \pm 0.001$	$-0.056 \pm 0.003$
M5	1458	2327	$+0.006 \pm 0.007$	$+0.001 \pm 0.001$	$-0.004 \pm 0.001$	$-0.014 \pm 0.001$	$+0.013 \pm 0.004$
M13	3225	3226	$-0.003 \pm 0.005$	$-0.020 \pm 0.001$	$-0.023 \pm 0.002$	$-0.006 \pm 0.002$	$-0.012 \pm 0.002$
M15	2566	1739	$+0.048 \pm 0.008$	$+0.020 \pm 0.002$	$+0.005 \pm 0.002$	$+0.000 \pm 0.002$	$-0.017 \pm 0.006$
M53	5390	5360	$-0.085 \pm 0.018$	$+0.000 \pm 0.002$	$+0.014 \pm 0.002$	$+0.017 \pm 0.003$	$+0.014 \pm 0.006$
M67	5935	5972	$+0.011 \pm 0.003$	$-0.001 \pm 0.002$	$-0.009 \pm 0.002$	$+0.004 \pm 0.002$	$-0.017 \pm 0.002$
M67	5935	6004	$-0.003 \pm 0.005$	$-0.004 \pm 0.002$	$-0.004 \pm 0.002$	$-0.004 \pm 0.002$	$-0.021 \pm 0.002$
M92	4682	5327	$+0.026 \pm 0.013$	$-0.009 \pm 0.002$	$-0.028 \pm 0.002$	$-0.040 \pm 0.002$	$-0.002 \pm 0.005$
NGC 2419	1402	1350	$+0.036 \pm 0.020$	$+0.026 \pm 0.002$	$+0.029 \pm 0.003$	$+0.033 \pm 0.002$	$+0.046 \pm 0.006$
NGC 2420	2888	3462	$-0.019 \pm 0.003$	$-0.001 \pm 0.001$	$-0.008 \pm 0.001$	$-0.002 \pm 0.001$	$+0.005 \pm 0.002$
NGC 2420	2888	3513	$+0.002 \pm 0.002$	$+0.005 \pm 0.001$	$-0.013 \pm 0.001$	$-0.003 \pm 0.001$	$+0.010 \pm 0.001$
NGC 4147	5381	5360	$+0.104 \pm 0.018$	$+0.006 \pm 0.004$	$+0.072 \pm 0.005$	$+0.045 \pm 0.005$	$+0.033 \pm 0.007$
NGC 5053	5390	5360	$+0.016 \pm 0.031$	$+0.027 \pm 0.004$	$+0.037 \pm 0.005$	$+0.002 \pm 0.005$	$+0.006 \pm 0.014$
NGC 5466	4623	4646	$+0.008 \pm 0.003$	$+0.019 \pm 0.001$	$+0.023 \pm 0.001$	$+0.009 \pm 0.001$	$+0.002 \pm 0.002$
NGC 6791	5416	5403	$-0.012 \pm 0.006$	$-0.053 \pm 0.001$	$-0.027 \pm 0.001$	$-0.047 \pm 0.001$	$-0.051 \pm 0.002$
NGC 6791	5416	6177	$-0.041 \pm 0.001$	$-0.035 \pm 0.000$	$-0.027 \pm 0.000$	$-0.032 \pm 0.000$	$-0.032 \pm 0.001$
Pal 4	5061	5071	...	$-0.021 \pm 0.006$	$+0.004 \pm 0.010$	$-0.017 \pm 0.006$	$+0.000 \pm 0.013$
Pal 14	4670	5323	$+0.017 \pm 0.031$	$+0.004 \pm 0.002$	$+0.007 \pm 0.002$	$-0.005 \pm 0.002$	$-0.002 \pm 0.005$
rms	...	...	0.042	0.021	0.027	0.024	0.026

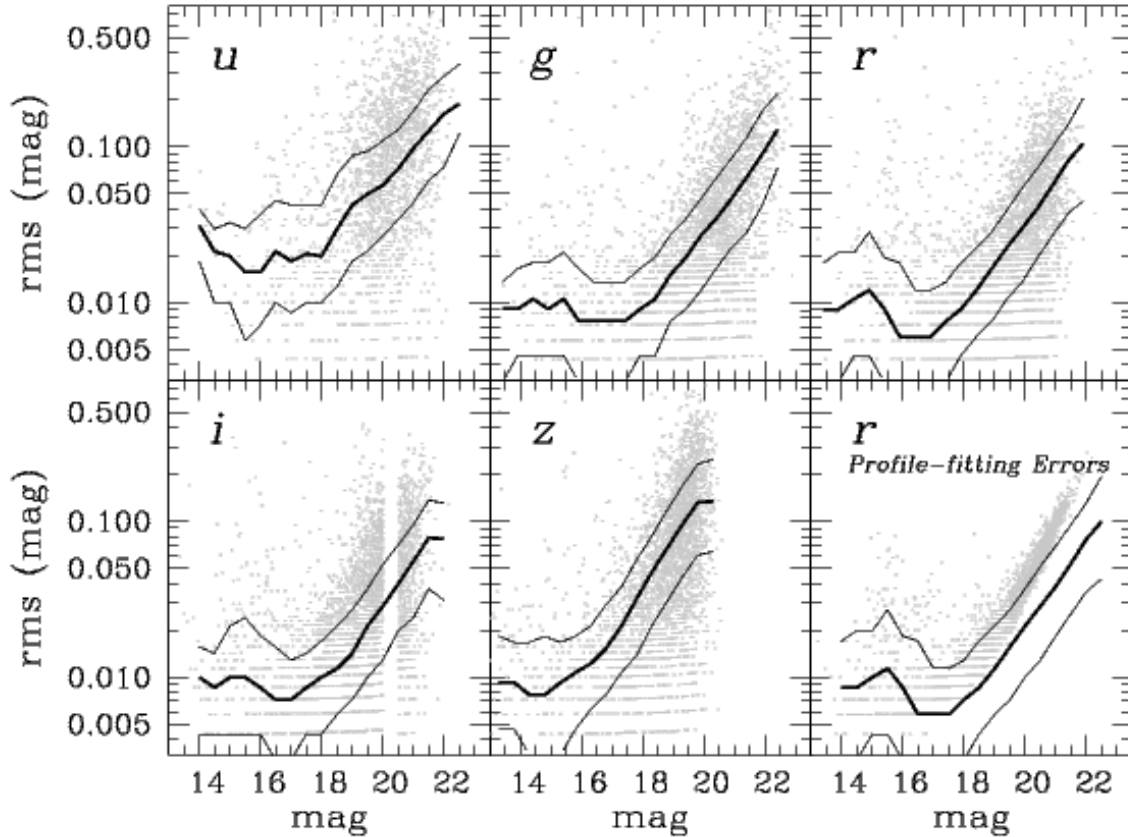


FIG. 8.— The rms magnitude errors from repeated flux measurements in overlapping strips in five bandpasses. For clarity, only 10% of points are shown. The thick solid line shows the median of these with intervals of 0.5 mag; thin lines on either side are the first and third quartiles. The bottom right panel compares the profile-fitting errors from DAOPHOT (*points*) to the same curves in the top right panel. Apparently discrete values on the y axis are due to round-off approximations.

measurements for stars that have been observed twice in overlapping strips. The thick solid line shows the median of these with intervals of 0.5 mag; thin lines on either side are the first and third quartiles. The error distributions at the bright ends indicate errors of  $\sim 1\%$  in *griz* and  $\sim 2\%$  in the *u* band, while the *Photo* magnitudes have 2% rms photometric precision for sources not limited by photon statistics (Ivezić et al. 2003). The photometric precision of DAOPHOT is about a factor of two better than that of *Photo*.

The bottom right panel in Figure 8 shows the reported DAOPHOT errors in the *r*-band. DAOPHOT estimates standard errors in the individual (instrumental) magnitudes, which are obtained either from the PSF profile-fitting residuals or from the star and sky flux measurements (Stetson et al. 2003). For stars observed in different strips, we estimated the standard error in the mean as  $1/\sigma^2 = \sum_i (1/\sigma_i)^2$ , where  $\sigma_i$  is the error reported from DAOPHOT, and multiplied it by the square root of the number of measurements ( $= 2$ ). As seen in Figure 8, most of the points are between the median and third quartile of the error distribution. Although DAOPHOT errors are slightly larger than the errors estimated from repeat measurements, they represent the approximate size of the errors well. The comparisons in other bands are similar to that in the *r* band.

#### 4.4. Comparison with *Photo* in Semi-Crowded Fields

The stellar densities in open cluster fields are significantly lower than in the cores of globular clusters, and *Photo* reports magnitudes for many objects. On the other hand, open cluster fields are more crowded than the typical high Galactic latitude fields in SDSS. Therefore, DAOPHOT magnitudes can be used to test the accuracy of the SDSS imaging pipelines near the Galactic plane, which is directly related to the quality assurance for the SEGUE imaging outputs. The systematic errors in these semi-crowded fields cannot be fully accounted for using the method based on the stellar locus (Ivezić et al. 2004) because the extinction corrections from Schlegel et al. (1998) become uncertain near the Galactic plane (Adelman-McCarthy et al. 2008).

In three open clusters in our sample, DAOPHOT detected  $\sim 100$ ,  $\sim 300$ , and  $\sim 1500$  sources in M67 ( $b = +31.9^\circ$ ), NGC 2420 ( $b = +19.6^\circ$ ), and NGC 6791 ( $b = +10.9^\circ$ ), respectively, with  $r < 20$  mag on each frame ( $10' \times 13'$ ). Stellar densities in NGC 2420 and NGC 6791 are about 2–10 times higher than the median density in the flanking fields for globular clusters, which is  $\sim 150$  per frame. *Photo* detected a comparable number of sources classified as STAR ( $\sim 80\%$ ). However, it is noted again that *Photo* failed to detect many stellar sources in fields near the globular cluster M71, where the stellar density is about four times higher than that of NGC 6791. We discuss the issue of M71 again in § 5.4.

While *Photo* detected a comparable number of stellar sources in the cluster fields, its photometry is less accurate than obtained in high Galactic latitude fields. Figure 9 shows differences between the DAOPHOT and the *Photo* magnitudes in one of the NGC 2420 runs, 2888–3–24/25/26. The comparisons are shown with no corrections on aa to DAOPHOT magnitudes. The spatial variations of the difference are stronger than those in the typical flanking fields for globular clusters (e.g., Fig. 3). The average rms differences from all of the open cluster runs are 0.016 mag, 0.028 mag, 0.021 mag, 0.023 mag, and 0.018 mag in *ugriz*, respectively. The rms values for *gri* are marginally larger than those from the globular cluster flanking fields. The most likely explana-

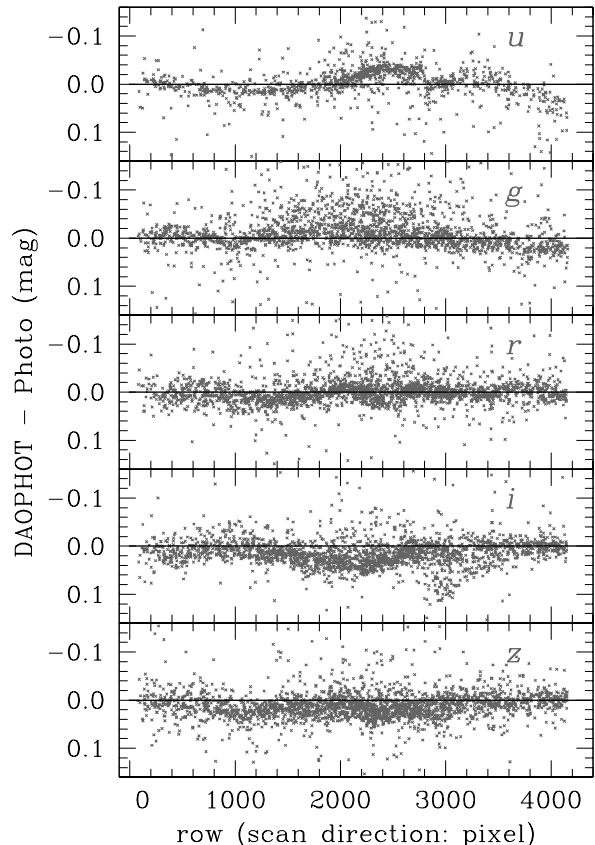


FIG. 9.— Comparison between the DAOPHOT and the *Photo* magnitudes in one of the NGC 2420 cluster fields. Comparisons are shown for *u*, *g*, *r*, *i*, and *z*, from the top to the bottom panels.

tion for the large differences is that *Photo* has trouble finding isolated bright objects for the PSF modeling in these semi-crowded fields. Thus, caution should be used for *Photo* results in open clusters and for those in low Galactic latitude fields.

## 5. RESULTS

In this section we present the DAOPHOT/ALLFRAME photometry for 20 clusters and derive cluster fiducial sequences over a wide range of metal abundances,  $\Delta \log(Z/Z_\odot) \sim 3$  dex. We then use these fiducial sequences to perform a preliminary test of theoretical isochrones, and to compare with fiducial sequences in *u'g'r'i'z'* from Clem et al. (2008).

### 5.1. Value-Added Catalog for DAOPHOT Cluster Photometry

We present the cluster photometry for this paper as a SDSS value-added catalog.<sup>22</sup> There is a file for each cluster for each run, labeled `cluster_run.phot`. For example, the M92 data are in `m92_4682.phot` and `m92_5327.phot`. Table 8 lists the columns of data. We note that the DAOPHOT identification number is unique for each cluster/run combination, and that the *x* and *y* pixel positions are for the tiled images. We flag saturated stars, i.e., those stars, which have a pixel set to 65000 DN within a 10 pixel radius from a stellar centroid. Although DAOPHOT will determine magnitudes for these stars based on the non-saturated pixels, these magnitudes should be treated with extreme caution. The flag is

<sup>22</sup> Available at [http://www.sdss.org/dr6/products/value\\_added/anjoh](http://www.sdss.org/dr6/products/value_added/anjoh)

TABLE 8  
QUANTITIES IN THE VALUE-ADDED DAOPHOT PHOTOMETRIC  
CATALOG

Column	Description
Run	SDSS Run number
ReRun	SDSS ReRun number
CamCol	SDSS CamCol 1-6
DAOPHOTID	DAOPHOT ID number
RA	RA (J2000) in deg
DEC	DEC (J2000) in deg
x_u	$u$ band x pixel (9999.99 = no detection)
y_u	$u$ band y pixel
u	$u$ DAOPHOT magnitude (99.999 = no detection) in mag
uErr	$u$ band magnitude error in mag
chi	DAOPHOT $\chi$ for $u$ band
sharp	DAOPHOT sharp for $u$ band
flag	0=ok, 1=near saturated pixel, 9=no detection in $u$ band
x_g	$g$ band x pixel (9999.99 = no detection)
y_g	$g$ band y pixel
g	$g$ DAOPHOT magnitude (99.999 = no detection) in mag
gErr	$g$ band magnitude error in mag
chi	DAOPHOT $\chi$ for $g$ band
sharp	DAOPHOT sharp for $g$ band
flag	0=ok, 1=near saturated pixel, 9=no detection in $g$ band
x_r	$r$ band x pixel (9999.99 = no detection)
y_r	$r$ band y pixel
r	$r$ DAOPHOT magnitude (99.999 = no detection) in mag
rErr	$r$ band magnitude error in mag
chi	DAOPHOT $\chi$ for $r$ band
sharp	DAOPHOT sharp for $r$ band
flag	0=ok, 1=near saturated pixel, 9=no detection in $r$ band
x_i	$i$ band x pixel (9999.99 = no detection)
y_i	$i$ band y pixel
i	$i$ DAOPHOT magnitude (99.999 = no detection) in mag
iErr	$i$ band magnitude error in mag
chi	DAOPHOT $\chi$ for $i$ band
sharp	DAOPHOT sharp for $i$ band
flag	0=ok, 1=near saturated pixel, 9=no detection in $i$ band
x_z	$z$ band x pixel (9999.99 = no detection)
y_z	$z$ band y pixel
z	$z$ DAOPHOT magnitude (99.999 = no detection) in mag
zErr	$z$ band magnitude error in mag
chi	DAOPHOT $\chi$ for $z$ band
sharp	DAOPHOT sharp for $z$ band
flag	0=ok, 1=near saturated pixel, 9=no detection in $z$ band

set to 1 if the star is near a saturated pixel, 9 if the star is not detected in a given frame, and 0 otherwise.

Figures 10 and 11 show CMDs of M3 and M92, respectively, with  $u-g$ ,  $g-r$ ,  $g-i$ , and  $g-z$  as color indices, and  $r$  as a luminosity index; hereafter  $(u-g, r)$ ,  $(g-r, r)$ ,  $(g-i, r)$ , and  $(g-z, r)$ , respectively. The  $(g-r, r)$  CMDs for all analyzed clusters are shown in Figures 12-16. Stars brighter than  $r \sim 14$  mag are saturated in the SDSS CCDs, so the brightest portions of the RGB are not seen in many cluster CMDs. A detailed description on the data and fiducial sequences is presented in the following section.

RR Lyraes show the most notable variations of fluxes in globular cluster studies. This can be seen in Figures 10-15, where RR Lyraes are scattered off the HBs, because most of them were observed only once in SDSS. They also stand out with large rms magnitude errors in the repeat flux measurements at  $r \sim 16$  mag (Fig. 8).

### 5.2. Cluster Fiducial Sequences

The individual points in Figures 10-16 are those stars that satisfy  $\chi$  and sharp index selection criteria in § 4.2. To identify stars in less-crowded regions, we further used the separation index (Stetson et al. 2003), which is defined as the logarithmic ratio of the surface brightness of a star to the

summed brightness from all neighboring stars. We followed the detailed procedure of computing a separation index in Clem et al. (2008). That is, we assumed the Moffat stellar profile of the surface brightness and considered the light contribution from those stars lying within 10 times the assumed FWHM in the  $r$ -band images. We adopted  $1.4''$  for the typical FWHM seeing for all fields using RunQA (Ivezić et al. 2004). In most of the cases we accepted those stars with a separation index larger than 3.5 dex. For M71 we used stars with a separation index larger than 2 dex, which produces the best looking sequences on the CMDs. However, we did not apply the above criterion based on the separation index for the relatively sparse clusters NGC 4147, NGC 7006, Pal 3, Pal 4, Pal 5, and Pal 14.

Given the  $\sim 2\%$  zero-point differences between different runs, we adjusted the zero point for the photometry in one of the runs to match the others before combining them together. Our selected runs for the local photometric standards are listed in the second column of Table 7. To reduce the contamination from background stars, we selected stars within a  $2.5'$  radius from a cluster center for Pal 3, Pal 4, and NGC 7006, those within a  $5.0'$  radius for NGC 6791, and Pal 5, and those within a  $2.0'$  for M71.

The curves in Figures 10-16 represent cluster fiducial sequences derived from the above data sample. A cluster fiducial sequence is defined as the locus of the number density peaks on a CMD. Representing a color-magnitude relation for single stars in a cluster, fiducial sequences can be used to derive relative distances to stars and star clusters and to test theoretical stellar isochrones. However, most of Galactic clusters lack a complete census of cluster membership and binarity, and the observed CMDs typically contain a non-uniform distribution of foreground/background stars and cluster binaries. In particular, low mass-ratio binaries are difficult to identify because their colors and magnitudes are similar to those of single stars. Therefore, careful selection of data points is required in order to derive accurate cluster fiducial sequences.

We adopted a photometric filtering scheme, as in An et al. (2007b, see also An et al. 2007a), in order to reduce the number of cluster binaries and non-cluster members in the CMDs. The photometric filtering is an automated process with a least amount of human intervention. The filtering process iteratively identifies the MS, SGB, and RGB ridgelines independently of the isochrones, determines the spread of points, and rejects stars if they are too far away from the ridgeline for a given magnitude. We combined the results from  $(g-r, r)$ ,  $(g-i, r)$ , and  $(g-z, r)$ , and rejected stars if they were tagged as an outlier at least in one of the CMDs. We started with a  $3\sigma$  rejection and reduced the threshold until it was limited to  $2.5\sigma$ . About 20% of stars were rejected from each set of CMDs, including cluster HB stars. For extremely sparse clusters (Pal 3, Pal 4, and Pal 14), we handpicked probable single star members from  $(g-r, r)$ ,  $(g-i, r)$ , and  $(g-z, r)$ .

Although a cluster ridgeline was obtained as a by-product from the photometric filtering, it has many small scale structures, which are mostly not physical. To obtain a smooth cluster sequence we used wider magnitude bins and estimated median colors in the last stage of the filtering process. We adjusted the magnitude bin size to adequately follow the shapes of the MS, SGB, and RGB, and smoothed the curve by averaging each point with a linear interpolation between adjacent points.

Although the above method worked well in most of the cases, it often showed a deviation at the top of the RGB for

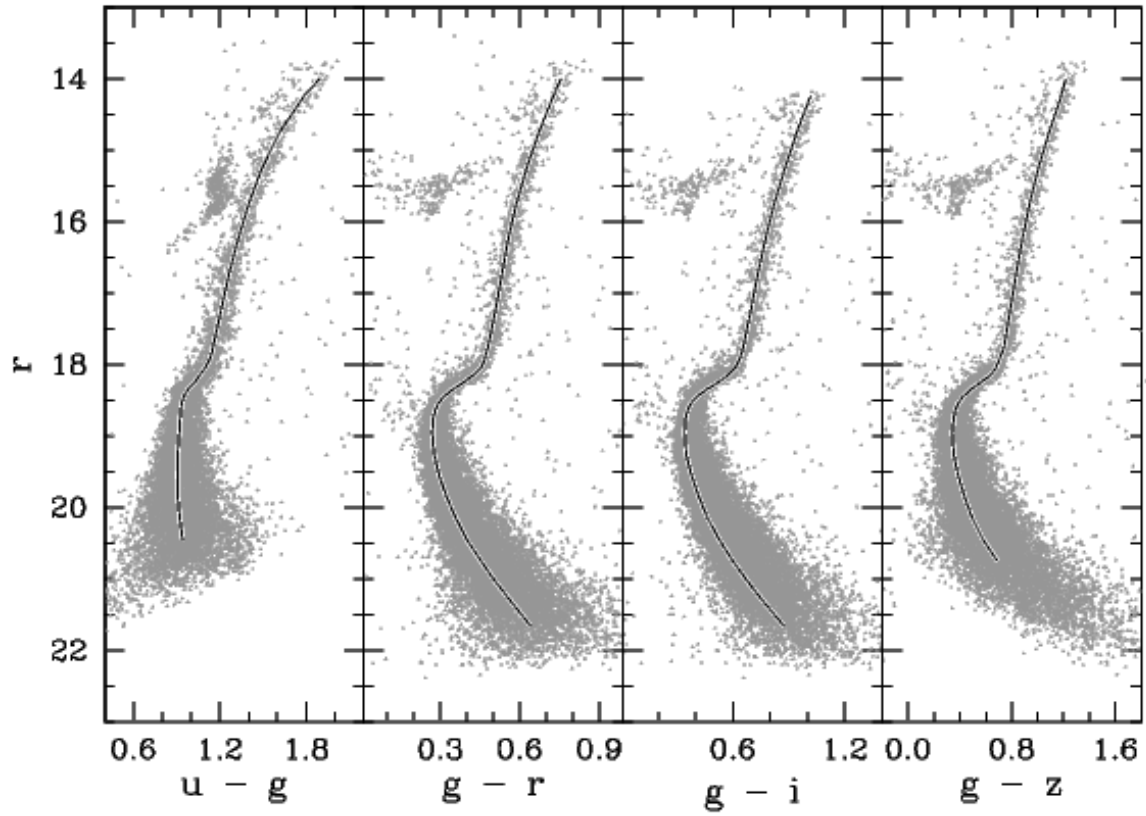


FIG. 10.— CMDs for M3. The points represent stars that passed the selection criteria based on the  $\chi$ , sharp, and separation indices (see text). The solid lines are the cluster fiducial sequences. Cluster RR Lyraes are scattered off the horizontal branch.

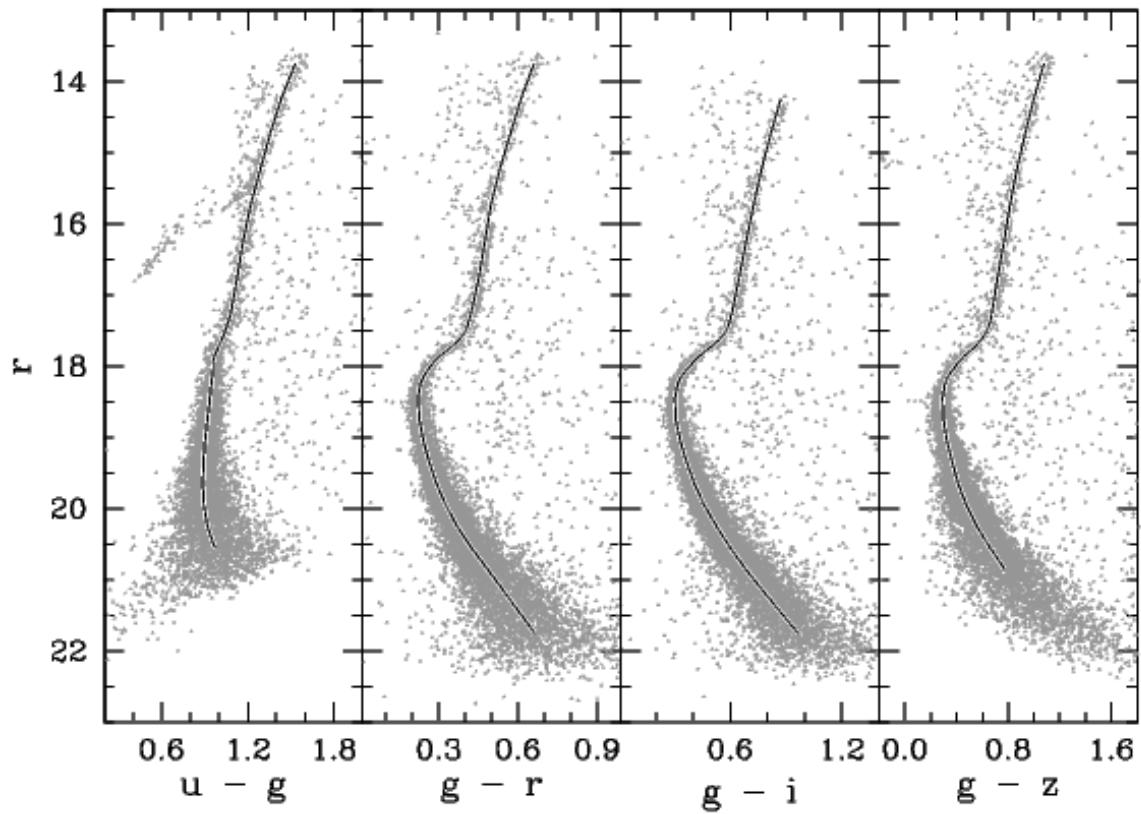


FIG. 11.— Same as in Fig. 10, but for M92.

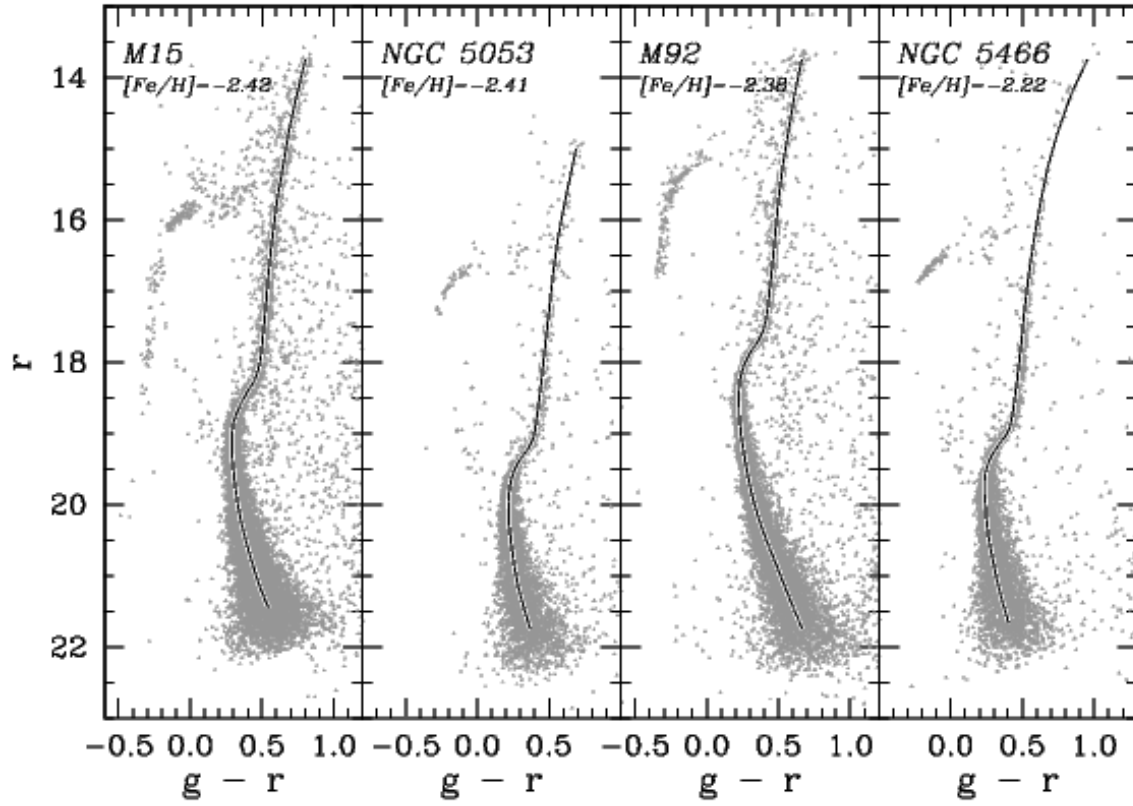


FIG. 12.— CMDs for clusters with  $[Fe/H] < -2.2$  with  $g-r$  as color indices. Points are stars that passed the selection criteria based on the  $\chi$ , sharp, and separation indices (see text).

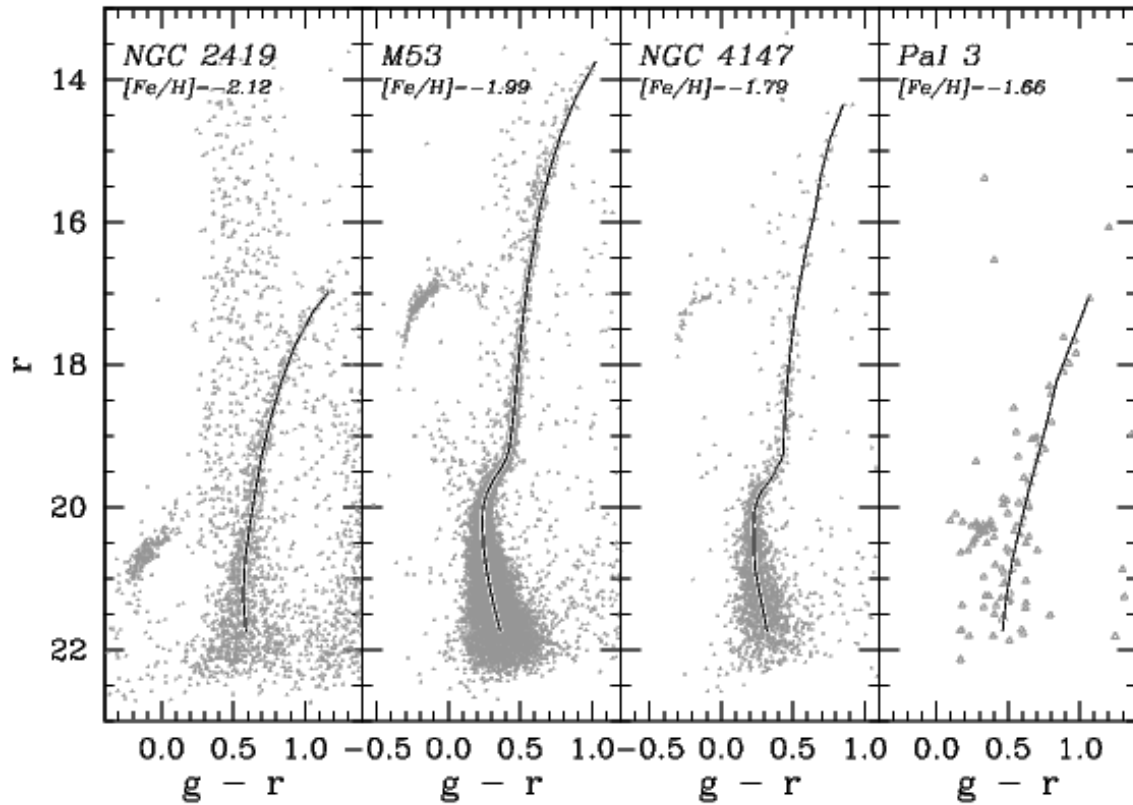


FIG. 13.— Same as in Fig. 12, but for clusters with  $-2.2 < [Fe/H] < -1.65$ . A separation index was not used to filter data for Pal 3.

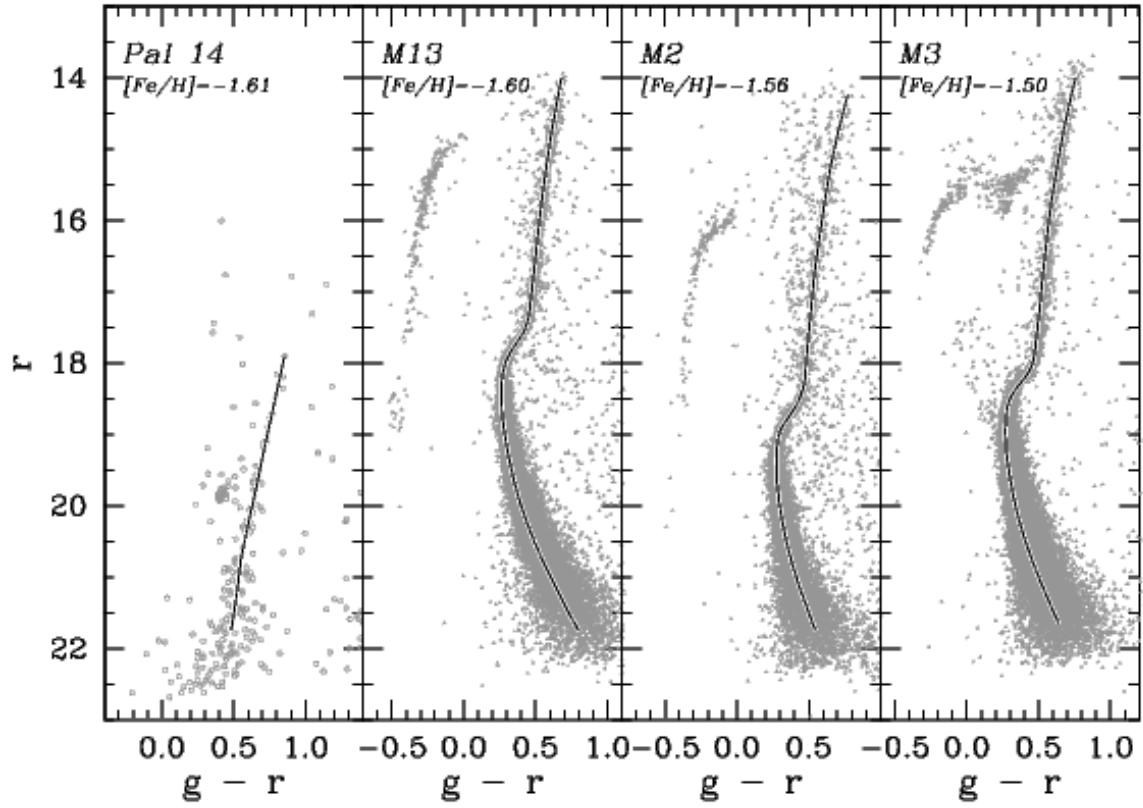


FIG. 14.— Same as in Fig. 12, but for clusters with  $-1.65 < [Fe/H] \leq -1.50$ . A separation index was not used to filter data for Pal 14.

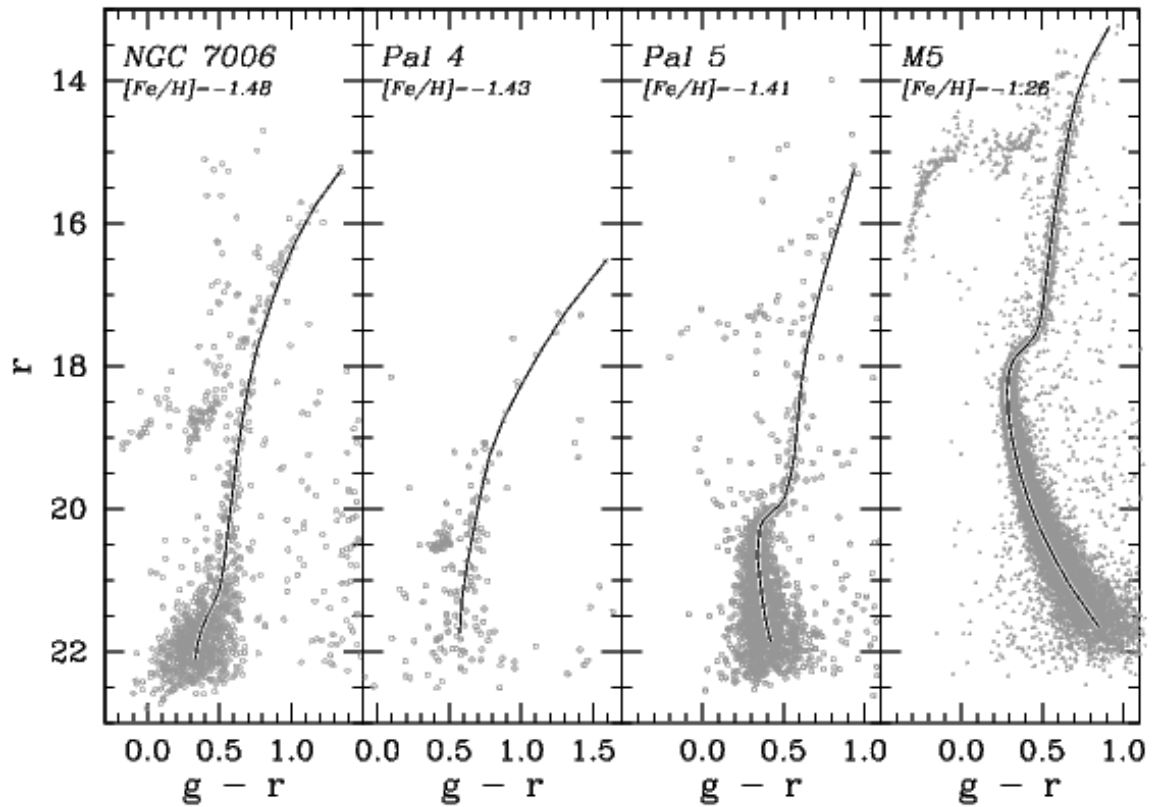


FIG. 15.— Same as in Fig. 12, but for clusters with  $-1.5 < [Fe/H] < -1.0$ . A separation index was not used to filter data except for M5.

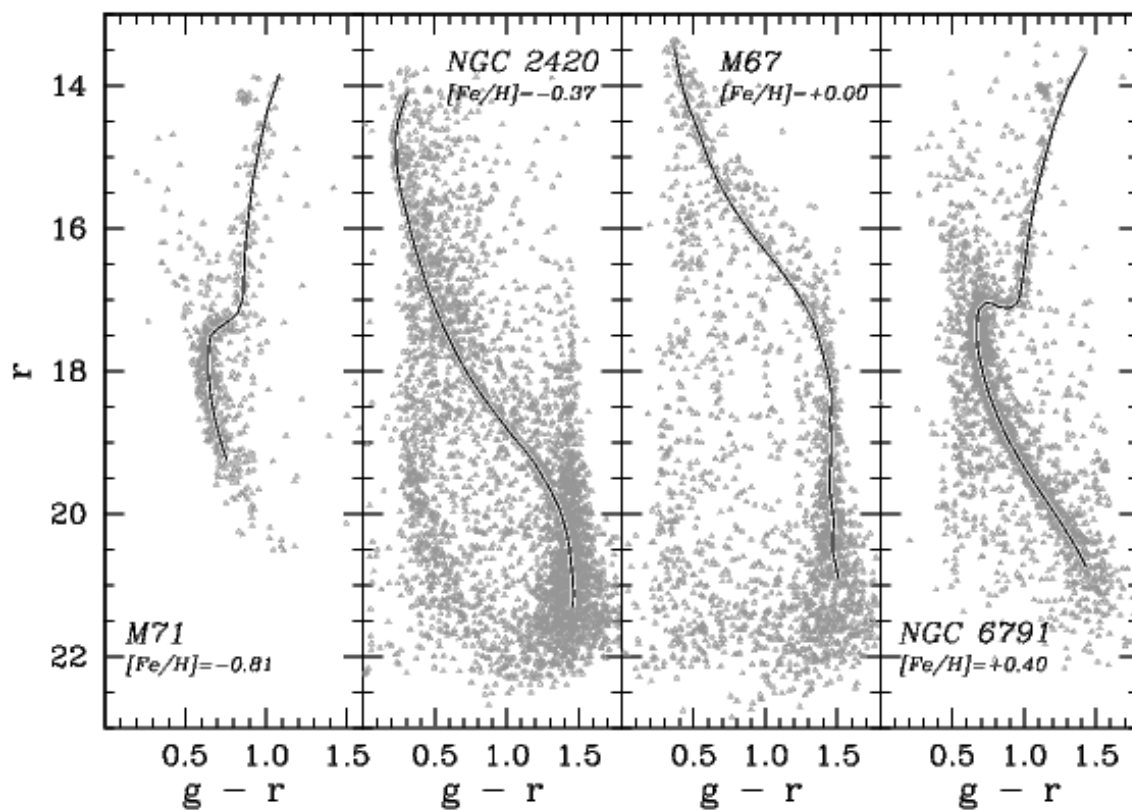


FIG. 16.— Same as in Fig. 12, but for clusters with  $[Fe/H] > -1.0$ .

TABLE 9  
FIDUCIAL SEQUENCES FOR NGC 2419

$r$	$u-g$	$g-r$	$g-i$	$g-z$
17.000	2.657	1.160	1.657	1.938
17.250	2.433	1.058	1.505	1.765
17.750	2.154	0.925	1.315	1.536
18.250	1.929	0.832	1.188	1.383
18.750	1.750	0.760	1.086	1.265
19.250	1.622	0.701	1.006	1.168
19.750	1.480	0.655	0.941	1.091
20.250	1.328	0.615	0.881	1.025
20.750	1.179	0.580	0.826	0.976
21.250	...	0.567	0.784	...
21.750	...	0.588	0.776	...

TABLE 10  
FIDUCIAL SEQUENCES FOR NGC 2420

$r$	$u-g$	$g-r$	$g-i$	$g-z$
14.100	1.162	0.310	0.382	0.384
14.300	1.150	0.273	0.343	0.333
14.500	1.133	0.245	0.308	0.292
14.700	1.122	0.229	0.285	0.271
14.900	1.113	0.229	0.282	0.268
15.100	1.108	0.235	0.291	0.275
15.300	1.104	0.246	0.311	0.297
15.500	1.100	0.265	0.339	0.333
15.700	1.103	0.290	0.373	0.375
15.900	1.115	0.315	0.408	0.417
16.100	1.133	0.340	0.445	0.462
16.300	1.159	0.367	0.482	0.512
16.500	1.191	0.398	0.523	0.562
16.700	1.230	0.429	0.566	0.614
16.900	1.287	0.463	0.614	0.670
17.100	1.362	0.500	0.667	0.734
17.300	1.449	0.539	0.723	0.804
17.500	1.551	0.586	0.788	0.882
17.700	1.663	0.636	0.857	0.966
17.900	1.777	0.689	0.926	1.051
18.100	1.903	0.748	1.003	1.144
18.300	2.016	0.812	1.094	1.255
18.500	2.129	0.884	1.194	1.375
18.700	2.294	0.958	1.294	1.488
18.900	...	1.035	1.404	1.609
19.100	...	1.120	1.531	1.758
19.300	...	1.195	1.651	1.904
19.500	...	1.255	1.748	2.027
19.700	...	1.312	1.842	2.153
19.900	...	1.360	1.942	2.284
20.100	...	1.394	2.032	2.398
20.300	...	1.422	2.107	2.489
20.500	...	1.438	2.179	2.575
20.700	...	1.446	2.249	2.678
20.900	...	1.457	2.309	2.777
21.100	...	1.464	2.353	2.851
21.300	...	1.462	2.389	2.928

sparsely populated clusters (e.g., NGC 4147, Pal 5). We adjusted these sequences by hand to match the observed RGB. In addition, we drew by hand the SGB of NGC 6791, which exhibits double color peaks at a given  $r$  magnitude. Fiducial sequences for the 20 clusters in our study are provided in Tables 9-28.

TABLE 11  
FIDUCIAL SEQUENCES FOR M67  
(NGC 2682)

$r$	$u-g$	$g-r$	$g-i$	$g-z$
13.500	1.246	0.369	...	0.499
13.700	1.256	0.388	0.522	0.535
13.900	1.287	0.408	0.539	0.569
14.100	1.327	0.431	0.566	0.612
14.300	1.378	0.465	0.610	0.663
14.500	1.444	0.507	0.665	0.719
14.700	1.519	0.545	0.719	0.785
14.900	1.601	0.579	0.766	0.849
15.100	1.692	0.616	0.816	0.911
15.300	1.794	0.661	0.878	0.992
15.500	1.896	0.713	0.949	1.082
15.700	2.011	0.772	1.036	1.186
15.900	2.143	0.841	1.136	1.303
16.100	2.259	0.912	1.230	1.406
16.300	2.368	0.988	1.338	1.535
16.500	2.467	1.070	1.465	1.696
16.700	2.533	1.147	1.578	1.828
16.900	2.591	1.216	1.674	1.943
17.100	2.638	1.279	1.773	2.066
17.300	2.660	1.330	1.866	2.182
17.500	2.655	1.363	1.953	2.297
17.700	2.628	1.392	2.048	2.422
17.900	2.625	1.419	2.130	2.539
18.100	2.655	1.440	2.188	2.628
18.300	...	1.455	2.241	2.704
18.500	...	1.454	2.292	2.776
18.700	...	1.448	2.339	2.841
18.900	...	1.458	2.387	2.908
19.100	...	1.460	2.430	2.974
19.300	...	1.451	2.474	3.043
19.500	...	1.445	2.520	3.116
19.700	...	1.447	2.569	3.189
19.900	...	1.463	2.612	3.253
20.100	...	1.476	2.635	3.285
20.300	...	1.467	2.671	3.338
20.500	...	1.464	2.711	3.415
20.700	...	1.487	2.714	3.417
20.900	...	1.505	2.680	3.333

TABLE 12  
FIDUCIAL SEQUENCES FOR PAL 3

$r$	$u-g$	$g-r$	$g-i$	$g-z$
17.071	2.431	1.059	1.461	1.697
17.750	2.231	0.929	1.309	1.528
18.250	2.079	0.836	1.189	1.388
18.750	1.915	0.777	1.097	1.271
19.250	1.682	0.712	1.018	1.154
19.750	1.485	0.643	0.945	1.055
20.250	1.376	0.585	0.882	0.999
20.750	...	0.528	0.805	0.944
21.250	...	0.487	0.709	0.929
21.750	...	0.461	0.598	...

TABLE 13  
FIDUCIAL SEQUENCES FOR PAL 4

$r$	$u-g$	$g-r$	$g-i$	$g-z$
16.526	3.305	1.589	2.416	2.800
17.250	3.224	1.307	1.915	2.225
17.750	3.014	1.149	1.641	1.905
18.250	2.662	1.005	1.418	1.645
18.750	2.346	0.876	1.230	1.419
19.250	2.099	0.781	1.094	1.252
19.750	1.858	0.722	1.013	1.166
20.250	1.564	0.673	0.951	1.092
20.750	...	0.627	0.884	1.050
21.250	...	0.589	0.820	1.105
21.750	...	0.573	0.793	1.201

TABLE 14  
FIDUCIAL SEQUENCES FOR NGC 4147

$r$	$u-g$	$g-r$	$g-i$	$g-z$
14.350	2.250	0.850	1.160	1.450
14.850	2.010	0.757	1.079	1.289
15.350	1.819	0.696	1.016	1.187
15.850	1.676	0.652	0.959	1.121
16.350	1.546	0.597	0.892	1.046
16.850	1.451	0.548	0.822	0.964
17.350	1.387	0.511	0.757	0.891
17.850	1.321	0.480	0.705	0.828
18.350	1.255	0.457	0.671	0.776
18.850	1.189	0.440	0.643	0.735
19.150	1.132	0.435	0.624	0.702
19.250	1.122	0.432	0.612	0.685
19.350	1.134	0.414	0.582	0.659
19.450	1.140	0.386	0.546	0.620
19.550	1.107	0.363	0.526	0.578
19.650	1.055	0.331	0.491	0.518
19.750	1.024	0.291	0.433	0.447
19.850	0.995	0.263	0.389	0.407
19.950	0.980	0.244	0.359	0.378
20.050	0.983	0.232	0.337	0.342
20.250	0.959	0.224	0.318	0.316
20.550	0.921	0.227	0.313	0.322
20.850	0.888	0.236	0.331	0.358
21.150	...	0.261	0.370	0.445
21.450	...	0.293	0.413	...
21.750	...	0.319	0.455	...

TABLE 15  
FIDUCIAL SEQUENCES FOR M53  
(NGC 5024)

$r$	$u-g$	$g-r$	$g-i$	$g-z$
13.750	2.461	1.026	...	1.707
14.250	2.117	0.890	1.254	1.479
14.750	1.869	0.788	1.132	1.313
15.250	1.686	0.708	1.022	1.193
15.750	1.539	0.645	0.936	1.093
16.250	1.422	0.600	0.871	1.015
16.750	1.328	0.560	0.816	0.947
17.250	1.254	0.525	0.765	0.887
17.750	1.190	0.497	0.724	0.837
18.250	1.137	0.475	0.692	0.794
18.750	1.087	0.451	0.658	0.751
19.150	1.034	0.425	0.621	0.708
19.250	1.014	0.414	0.605	0.689
19.350	0.989	0.397	0.576	0.657
19.450	0.963	0.369	0.532	0.606
19.550	0.938	0.334	0.479	0.537
19.650	0.915	0.305	0.431	0.468
19.750	0.897	0.280	0.393	0.414
19.850	0.890	0.260	0.362	0.375
19.950	0.894	0.247	0.339	0.351
20.050	0.895	0.239	0.327	0.341
20.250	0.877	0.235	0.324	0.343
20.550	0.845	0.243	0.335	0.373
20.850	0.809	0.263	0.360	0.433
21.150	...	0.291	0.400	...
21.450	...	0.324	0.453	...
21.750	...	0.362	0.510	...

TABLE 16  
FIDUCIAL SEQUENCES FOR NGC 5053

$r$	$u-g$	$g-r$	$g-i$	$g-z$
15.000	1.555	0.688	0.995	1.133
15.750	1.404	0.611	0.881	1.011
16.250	1.313	0.564	0.818	0.942
16.750	1.235	0.530	0.770	0.883
17.250	1.167	0.501	0.727	0.828
17.750	1.113	0.474	0.689	0.781
18.250	1.067	0.447	0.651	0.738
18.750	1.026	0.417	0.605	0.682
18.850	1.015	0.410	0.595	0.664
18.950	0.998	0.403	0.584	0.635
19.050	0.968	0.393	0.566	0.607
19.150	0.934	0.371	0.532	0.586
19.250	0.929	0.340	0.483	0.541
19.350	0.928	0.303	0.427	0.471
19.450	0.913	0.274	0.381	0.407
19.550	0.905	0.254	0.347	0.360
19.650	0.896	0.237	0.322	0.317
19.750	0.886	0.225	0.308	0.293
19.950	0.878	0.215	0.296	0.293
20.250	0.864	0.218	0.297	0.313
20.550	0.849	0.234	0.319	0.339
20.850	0.822	0.256	0.354	0.382
21.150	0.796	0.284	0.397	0.452
21.450	...	0.323	0.448	...
21.750	...	0.369	0.508	...

TABLE 17  
FIDUCIAL SEQUENCES FOR M3  
(NGC 5272)

$r$	$u-g$	$g-r$	$g-i$	$g-z$
14.000	1.895	0.756	...	1.219
14.250	1.784	0.726	1.015	1.178
14.750	1.616	0.673	0.943	1.089
15.250	1.494	0.627	0.878	1.007
15.750	1.402	0.587	0.821	0.938
16.250	1.327	0.556	0.773	0.882
16.750	1.262	0.531	0.733	0.833
17.250	1.208	0.507	0.696	0.787
17.750	1.154	0.480	0.656	0.742
17.850	1.143	0.473	0.646	0.724
17.950	1.126	0.465	0.633	0.701
18.050	1.096	0.451	0.612	0.678
18.150	1.061	0.424	0.575	0.635
18.250	1.022	0.387	0.521	0.561
18.350	0.979	0.346	0.458	0.483
18.450	0.948	0.312	0.406	0.424
18.550	0.935	0.291	0.374	0.387
18.650	0.929	0.279	0.355	0.364
18.750	0.926	0.273	0.345	0.350
18.950	0.919	0.269	0.339	0.340
19.250	0.908	0.275	0.348	0.352
19.550	0.904	0.295	0.376	0.386
19.850	0.908	0.322	0.416	0.436
20.150	0.921	0.357	0.464	0.496
20.450	0.942	0.400	0.526	0.580
20.750	...	0.451	0.599	0.690
21.050	...	0.509	0.682	...
21.350	...	0.574	0.775	...
21.650	...	0.640	0.872	...

TABLE 19  
FIDUCIAL SEQUENCES FOR PAL 5

$r$	$u-g$	$g-r$	$g-i$	$g-z$
15.250	2.236	0.935	1.332	1.560
15.750	2.158	0.879	1.258	1.481
16.250	2.020	0.811	1.169	1.376
16.750	1.833	0.749	1.081	1.271
17.250	1.636	0.694	1.000	1.174
17.750	1.513	0.644	0.929	1.086
18.250	1.440	0.610	0.873	1.012
18.750	1.349	0.587	0.834	0.956
19.250	1.267	0.566	0.802	0.928
19.550	1.268	0.543	0.776	0.905
19.650	1.297	0.530	0.754	0.886
19.750	1.278	0.519	0.727	0.860
19.850	1.188	0.507	0.705	0.803
19.950	1.117	0.474	0.661	0.723
20.050	1.088	0.424	0.588	0.657
20.150	1.072	0.380	0.517	0.599
20.250	1.047	0.357	0.484	0.551
20.350	1.028	0.351	0.475	0.528
20.450	1.015	0.346	0.466	0.527
20.650	0.975	0.339	0.460	0.531
20.950	0.921	0.352	0.468	0.526
21.250	...	0.368	0.496	...
21.550	...	0.388	0.538	...
21.850	...	0.418	0.587	...

TABLE 20  
FIDUCIAL SEQUENCES FOR M5  
(NGC 5904)

$r$	$u-g$	$g-r$	$g-i$	$g-z$
13.250	2.047	0.915	...	1.395
13.750	1.885	0.792	...	1.295
14.250	1.745	0.710	1.017	1.190
14.750	1.631	0.661	0.951	1.094
15.250	1.528	0.621	0.891	1.016
15.750	1.444	0.584	0.838	0.953
16.250	1.378	0.552	0.794	0.901
16.750	1.321	0.525	0.756	0.855
17.250	1.271	0.498	0.717	0.808
17.250	1.271	0.498	0.717	0.808
17.350	1.253	0.490	0.709	0.794
17.450	1.229	0.477	0.693	0.774
17.550	1.203	0.459	0.662	0.737
17.650	1.155	0.429	0.616	0.680
17.750	1.089	0.386	0.554	0.604
17.850	1.040	0.343	0.492	0.530
17.950	1.017	0.315	0.450	0.475
18.050	1.006	0.299	0.427	0.444
18.150	0.999	0.290	0.415	0.429
18.350	0.986	0.284	0.406	0.420
18.650	0.976	0.290	0.414	0.428
18.950	0.975	0.308	0.439	0.456
19.250	0.983	0.335	0.478	0.502
19.550	1.012	0.368	0.527	0.560
19.850	1.068	0.411	0.589	0.635
20.150	1.140	0.463	0.662	0.725
20.450	1.218	0.522	0.746	0.831
20.750	...	0.588	0.841	0.950
21.050	...	0.665	0.949	...
21.350	...	0.754	1.074	...
21.650	...	0.850	1.213	...

TABLE 18  
FIDUCIAL SEQUENCES FOR NGC 5466

$r$	$u-g$	$g-r$	$g-i$	$g-z$
13.750	2.227	0.954	1.366	1.576
14.250	1.918	0.839	1.197	1.386
14.750	1.707	0.748	1.072	1.241
15.250	1.556	0.679	0.976	1.128
15.750	1.430	0.625	0.898	1.034
16.250	1.340	0.582	0.840	0.961
16.750	1.262	0.545	0.786	0.897
17.250	1.195	0.514	0.738	0.840
17.750	1.145	0.491	0.701	0.795
18.250	1.099	0.465	0.662	0.747
18.750	1.046	0.429	0.609	0.681
18.750	1.046	0.429	0.609	0.681
18.850	1.034	0.419	0.595	0.658
18.950	1.016	0.406	0.570	0.621
19.050	0.981	0.378	0.526	0.568
19.150	0.947	0.338	0.469	0.503
19.250	0.925	0.302	0.418	0.435
19.350	0.912	0.275	0.378	0.381
19.450	0.903	0.255	0.348	0.349
19.550	0.897	0.243	0.328	0.331
19.650	0.895	0.237	0.316	0.320
19.850	0.891	0.237	0.312	0.318
20.150	0.870	0.245	0.322	0.338
20.450	0.848	0.263	0.347	0.384
20.750	0.831	0.289	0.387	0.469
21.050	...	0.320	0.437	0.589
21.350	...	0.358	0.493	...
21.650	...	0.402	0.551	...

TABLE 21  
FIDUCIAL SEQUENCES FOR PAL 14

$r$	$u-g$	$g-r$	$g-i$	$g-z$
17.905	2.009	0.854	1.221	1.441
18.250	1.915	0.817	1.180	1.368
18.750	1.865	0.760	1.110	1.280
19.250	1.766	0.706	1.030	1.201
19.750	1.626	0.655	0.949	1.120
20.250	...	0.600	0.879	1.031
20.750	...	0.550	0.816	0.956
21.250	...	0.521	0.777	0.944
21.750	...	0.484	0.775	...

TABLE 22  
FIDUCIAL SEQUENCES FOR M13  
(NGC 6205)

$r$	$u-g$	$g-r$	$g-i$	$g-z$
14.000	1.669	0.679	0.971	1.119
14.750	1.500	0.613	0.862	0.998
15.250	1.402	0.574	0.805	0.928
15.750	1.329	0.540	0.761	0.873
16.250	1.275	0.512	0.722	0.827
16.750	1.222	0.486	0.686	0.784
17.250	1.164	0.459	0.652	0.735
17.350	1.148	0.451	0.643	0.721
17.450	1.123	0.439	0.623	0.699
17.550	1.092	0.421	0.591	0.665
17.650	1.053	0.392	0.545	0.610
17.750	1.014	0.357	0.493	0.544
17.850	0.986	0.325	0.447	0.486
17.950	0.966	0.299	0.410	0.441
18.050	0.951	0.282	0.383	0.409
18.150	0.942	0.271	0.364	0.387
18.250	0.938	0.264	0.355	0.375
18.450	0.929	0.262	0.352	0.370
18.750	0.917	0.270	0.363	0.383
19.050	0.913	0.288	0.388	0.415
19.350	0.923	0.315	0.427	0.462
19.650	0.952	0.349	0.476	0.523
19.950	0.997	0.391	0.535	0.599
20.250	1.053	0.441	0.608	0.687
20.550	...	0.500	0.692	0.792
20.850	...	0.569	0.791	0.913
21.150	...	0.643	0.895	...
21.450	...	0.719	1.004	...
21.750	...	0.798	1.127	...

### 5.3. Preliminary Test of Theoretical Models

Girardi et al. (2004) provided the first extensive sets of theoretical isochrones in the  $ugriz$  system. They derived magnitudes in  $ugriz$  using ATLAS9 synthetic spectra (Castelli et al. 1997; Bessell et al. 1998) for most regions of  $T_{\text{eff}}$  and  $\log g$  space. Here we test the models constructed from the Girardi et al. (2000) evolutionary tracks with our fiducial sequences. Detailed comparisons to theoretical models will be presented in a companion paper (D. An et al. 2008, in preparation).

Isochrones in Girardi et al. (2004) were constructed for a perfect AB magnitude system, in which magnitudes can be translated directly into physical flux units. However, it is known that the SDSS photometry slightly deviates from a true AB system (Abazajian et al. 2004). To compare our fiducial sequences to the isochrones, we adjusted model magnitudes using AB corrections given by Eisenstein et al. (2006):  $u_{\text{AB}} = u - 0.040$ ,  $i_{\text{AB}} = i + 0.015$ , and  $z_{\text{AB}} = z + 0.030$ , with no

TABLE 23  
FIDUCIAL SEQUENCES FOR M92  
(NGC 6342)

$r$	$u-g$	$g-r$	$g-i$	$g-z$
13.750	1.531	0.661	...	1.079
14.250	1.432	0.612	0.870	1.000
14.750	1.355	0.570	0.816	0.929
15.250	1.285	0.530	0.766	0.867
15.750	1.220	0.497	0.724	0.814
16.250	1.169	0.474	0.685	0.766
16.750	1.125	0.451	0.649	0.720
17.250	1.081	0.422	0.609	0.675
17.350	1.070	0.415	0.598	0.664
17.450	1.053	0.408	0.586	0.647
17.550	1.034	0.394	0.567	0.622
17.650	1.015	0.371	0.532	0.584
17.750	0.992	0.341	0.485	0.529
17.850	0.970	0.308	0.437	0.466
17.950	0.958	0.280	0.397	0.412
18.050	0.955	0.258	0.364	0.369
18.150	0.952	0.242	0.336	0.333
18.250	0.948	0.230	0.317	0.310
18.450	0.936	0.221	0.302	0.292
18.750	0.918	0.225	0.307	0.299
19.050	0.903	0.240	0.329	0.326
19.350	0.891	0.263	0.363	0.365
19.650	0.886	0.291	0.405	0.414
19.950	0.894	0.326	0.458	0.477
20.250	0.919	0.369	0.523	0.557
20.550	0.969	0.422	0.597	0.657
20.850	...	0.483	0.682	0.771
21.150	...	0.544	0.774	...
21.450	...	0.604	0.869	...
21.750	...	0.664	0.964	...

TABLE 24  
FIDUCIAL SEQUENCES FOR NGC 6791

$r$	$u-g$	$g-r$	$g-i$	$g-z$
13.550	3.424	1.424	...	2.465
14.050	3.227	1.299	1.790	2.147
14.550	3.083	1.206	1.649	1.936
15.050	2.954	1.138	1.543	1.808
15.550	2.815	1.078	1.452	1.697
16.050	2.707	1.034	1.388	1.614
16.550	2.626	1.001	1.348	1.561
16.850	2.572	0.978	1.316	1.524
16.950	2.538	0.968	1.299	1.506
17.050	2.470	0.950	1.273	1.488
17.117	2.371	0.896	1.202	1.380
17.100	2.168	0.820	1.105	1.260
17.038	2.031	0.766	1.023	1.162
17.045	1.950	0.732	0.965	1.110
17.097	1.900	0.702	0.931	1.055
17.150	1.863	0.685	0.913	1.029
17.250	1.843	0.675	0.898	1.012
17.350	1.829	0.670	0.891	1.003
17.450	1.827	0.669	0.890	1.002
17.550	1.830	0.670	0.892	1.002
17.750	1.851	0.682	0.908	1.022
18.050	1.918	0.715	0.952	1.075
18.350	2.016	0.760	1.012	1.145
18.650	2.112	0.815	1.087	1.236
18.950	...	0.886	1.186	1.356
19.250	...	0.969	1.306	1.502
19.550	...	1.061	1.439	1.663
19.850	...	1.162	1.590	1.843
20.150	...	1.263	1.753	2.039
20.450	...	1.354	1.913	2.229
20.750	...	1.431	2.067	2.425

TABLE 25  
FIDUCIAL SEQUENCES FOR M71  
(NGC 6838)

$r$	$u-g$	$g-r$	$g-i$	$g-z$
13.850	2.464	1.080	9.000	1.879
14.350	2.294	1.010	1.500	1.766
14.850	2.170	0.959	1.433	1.681
15.350	2.074	0.919	1.374	1.616
15.850	1.991	0.890	1.337	1.566
16.350	1.927	0.871	1.309	1.523
16.850	1.871	0.859	1.276	1.487
16.987	1.854	0.857	1.268	1.478
17.200	1.821	0.822	1.240	1.420
17.267	1.776	0.790	1.204	1.373
17.362	1.634	0.730	1.111	1.272
17.443	1.508	0.682	1.045	1.183
17.514	1.456	0.659	1.019	1.140
17.650	1.444	0.650	1.000	1.124
17.750	1.441	0.647	0.991	1.122
17.850	1.437	0.645	0.989	1.123
18.050	1.437	0.645	0.992	1.129
18.350	1.477	0.658	1.006	1.151
18.650	1.540	0.683	1.040	1.193
18.950	1.601	0.716	1.098	1.265
19.250	1.675	0.757	1.171	1.357

TABLE 26  
FIDUCIAL SEQUENCES FOR NGC 7006

$r$	$u-g$	$g-r$	$g-i$	$g-z$
15.250	...	1.348	1.898	2.220
15.750	2.858	1.168	1.659	1.939
16.250	2.508	1.030	1.462	1.709
16.750	2.238	0.927	1.316	1.538
17.250	2.022	0.839	1.197	1.401
17.750	1.825	0.763	1.095	1.279
18.250	1.677	0.703	1.011	1.178
18.750	1.568	0.659	0.945	1.112
19.250	1.461	0.622	0.890	1.059
19.750	1.380	0.591	0.840	1.000
20.250	1.329	0.562	0.789	0.940
20.750	...	0.534	0.745	0.862
21.100	...	0.504	0.696	0.801
21.300	...	0.465	0.629	0.786
21.500	...	0.416	0.547	...
21.700	...	0.376	0.493	...
21.900	...	0.347	0.457	...
22.100	...	0.332	0.419	...

corrections in  $g$  and  $r$  (see also Holberg & Bergeron 2006).

We restricted our comparisons to five globular clusters (M3, M5, M13, M15, and M92) and one solar-metallicity open cluster (M67). These clusters not only have well-defined sequences but also have relatively well-studied distances and reddening estimates, which are necessary to infer the absolute magnitudes of stars. Furthermore, the metallicities of these clusters are well-studied, so the model colors can be tested more accurately for a given metallicity.

For globular clusters, we adopted the MS-fitting distances given by Kraft & Ivans (2003, see Table 1), which are based on measurements of *Hipparcos* subdwarfs. We also adopted reddening values from Kraft & Ivans (2003). For M67 we adopted cluster distance and reddening estimates from An et al. (2007b). The isochrone colors and magnitudes were corrected for the assumed reddening using theoretical computations of extinction coefficients ( $A_\lambda/A_V$ ) in Girardi et al. (2004). Specifically, we used their model flux calculation for

TABLE 27  
FIDUCIAL SEQUENCES FOR M15  
(NGC 7078)

$r$	$u-g$	$g-r$	$g-i$	$g-z$
13.750	1.776	0.803	...	1.401
14.250	1.645	0.743	1.100	1.291
14.750	1.531	0.689	1.016	1.200
15.250	1.442	0.645	0.949	1.126
15.750	1.363	0.604	0.890	1.054
16.250	1.294	0.571	0.843	0.995
16.750	1.236	0.546	0.806	0.951
17.250	1.188	0.523	0.771	0.910
17.750	1.148	0.500	0.734	0.857
17.950	1.137	0.490	0.718	0.833
18.050	1.123	0.480	0.702	0.818
18.150	1.092	0.465	0.678	0.791
18.250	1.073	0.448	0.651	0.757
18.350	1.063	0.420	0.612	0.707
18.450	1.044	0.387	0.562	0.648
18.550	1.025	0.360	0.523	0.604
18.650	1.015	0.337	0.486	0.561
18.750	1.016	0.315	0.449	0.513
18.850	1.016	0.300	0.427	0.485
19.050	1.003	0.289	0.413	0.470
19.350	0.987	0.291	0.415	0.470
19.650	0.973	0.306	0.435	0.493
19.950	0.960	0.328	0.468	0.533
20.250	0.941	0.355	0.506	0.586
20.550	0.916	0.391	0.556	0.665
20.850	...	0.434	0.622	0.772
21.150	...	0.484	0.697	...
21.450	...	0.543	0.772	...

TABLE 28  
FIDUCIAL SEQUENCES FOR M2  
(NGC 7089)

$r$	$u-g$	$g-r$	$g-i$	$g-z$
14.250	2.016	0.771	1.123	1.285
14.750	1.839	0.707	1.023	1.168
15.250	1.695	0.650	0.938	1.069
15.750	1.587	0.609	0.878	1.003
16.250	1.499	0.573	0.827	0.944
16.750	1.418	0.540	0.779	0.887
17.250	1.350	0.515	0.739	0.840
17.750	1.294	0.492	0.703	0.796
18.250	1.260	0.472	0.667	0.753
18.250	1.260	0.472	0.667	0.753
18.350	1.243	0.460	0.652	0.737
18.450	1.208	0.444	0.631	0.709
18.550	1.170	0.426	0.605	0.672
18.650	1.125	0.398	0.563	0.625
18.750	1.084	0.361	0.512	0.566
18.850	1.050	0.327	0.466	0.507
18.950	1.028	0.302	0.429	0.454
19.050	1.021	0.287	0.401	0.418
19.150	1.020	0.280	0.385	0.405
19.350	1.011	0.273	0.374	0.397
19.650	0.999	0.276	0.381	0.400
19.950	0.997	0.293	0.405	0.431
20.250	0.991	0.318	0.443	0.481
20.550	0.975	0.350	0.492	0.545
20.850	0.957	0.389	0.550	0.631
21.150	...	0.437	0.617	0.738
21.450	...	0.493	0.696	...
21.750	...	0.546	0.790	...

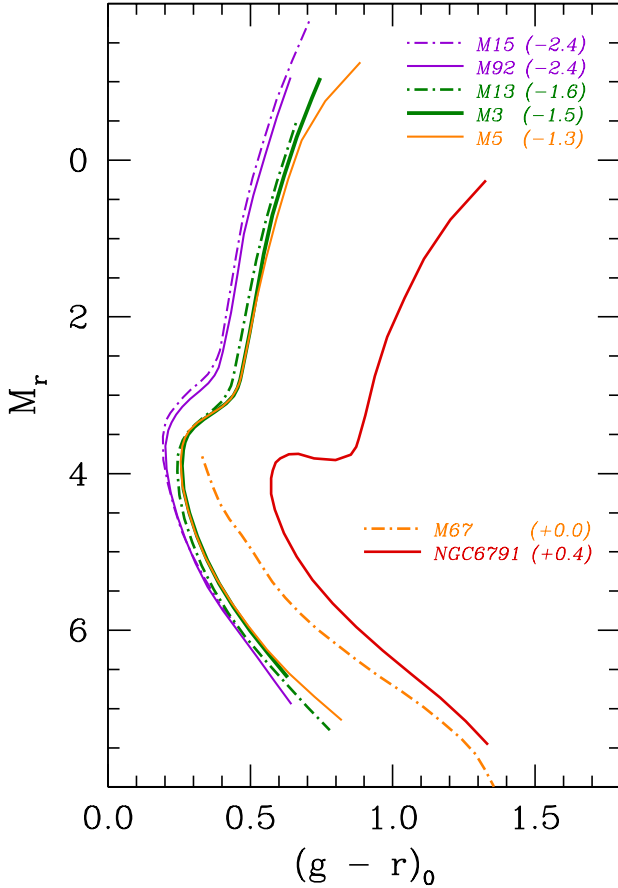


FIG. 17.— Composite CMDs in  $(g-r)_0$  vs  $M_r$  for five globular clusters (M3, M5, M13, M15, and M92) and two open clusters (M67 and NGC 6791). Their metal abundances are shown in parenthesis (see text for details).

dwarfs ( $T_{\text{eff}} = 5000$ ,  $\log g = 4.50$ ,  $[\text{m}/\text{H}] = 0$ ):  $A_u/A_V = 1.574$ ,  $A_g/A_V = 1.189$ ,  $A_r/A_V = 0.877$ ,  $A_i/A_V = 0.673$ , and  $A_z/A_V = 0.489$  where  $V$  represents the Johnson  $V$  filter. The differences in the extinction coefficients for different  $T_{\text{eff}}$ ,  $\log g$ , and  $[\text{m}/\text{H}]$  are negligible for our cluster sample with  $E(B-V) \leq 0.10$ . We assumed  $R_V \equiv A_V/E(B-V) = 3.1$  and derived extinction and color-excess values in  $ugriz$  for a given  $E(B-V)$ .

Figure 17 shows fiducial sequences for these clusters on the absolute magnitude  $M_r$  versus intrinsic color  $(g-r)_0$  space, with the above adopted distances and reddening values. We included a fiducial sequence for NGC 6791 in the plot, using its parameters in Table 2. These clusters cover a wide range of metal abundances ( $-2.4 < [\text{Fe}/\text{H}] < +0.4$ ); their fiducial sequences become redder at higher metallicities. In the figure, two groups of globular cluster sequences are distinguished by two different colors according to their metal abundances in Kraft & Ivans (2003): M15 and M92 ( $[\text{Fe}/\text{H}] \approx -2.4$ ; *violet*), M3 and M13 ( $[\text{Fe}/\text{H}] \approx -1.6$ ; *green*). Cluster sequences in each group of the clusters show  $\lesssim 2\%$  agreement in color. We note that these differences are within the expected size of the errors from the adopted distance, reddening, and photometric zero points (§ 4.2).

Figures 18 and 19 show comparisons between fiducial sequences for the two most metal-poor globular clusters in our sample, M15 and M92 (*dotted line*), and the Girardi et al. (2004) theoretical isochrones (*solid line*). Models are shown with the heavy-element content  $Z = 0.0001$  ( $[\text{m}/\text{H}] \approx -2.3$ ) at ages of 10.0, 11.2, 12.6, 14.1, and 15.9 Gyrs. Comparisons

in  $(g-r, r)$ ,  $(g-i, r)$ , and  $(g-z, r)$  show that model colors are  $\sim 0.02$ – $0.05$  mag bluer and redder than the fiducial sequences for MS and RGB, respectively. In addition, the morphology of the model SGB does not perfectly match the observed ones. A significant color offset is found in  $(u-g, r)$ , up to as large as  $\sim 0.1$  mag. While the SDSS  $u$ -band filters are known to have a red leak (Stoughton et al. 2002), it is probably not the reason for the discrepancy found for stars bluer than  $g-r \sim 1.2$ . We note again that our photometry does not reach to the tips of the RGBs in all clusters because of saturation, and that this work does not constrain the reddest part of the RGBs for the nearest clusters.

Figures 20 and 21 show comparisons for the intermediate metallicity globular clusters M13 and M3, respectively. The models are shown for two different metallicities,  $Z = 0.0004$  ( $[\text{m}/\text{H}] \approx -1.7$ ) and  $Z = 0.0010$  ( $[\text{m}/\text{H}] \approx -1.3$ ), to bracket the observed cluster abundances. It is noted that these models assume the scaled-solar abundance ratios, while metal-poor stars show  $\alpha$ -enhanced abundances (e.g., Sneden et al. 2004; Venn et al. 2004, and references therein). However, the effects of  $\alpha$ -enhancement can be mimicked by increasing the total metal abundance in this low metallicity range (Salaris et al. 1993; Kim et al. 2002; Cassisi et al. 2004). Nevertheless, neither isochrones simultaneously match the colors of both the MS and RGB sequences with high precision. We found a similar result for M5 ( $[\text{Fe}/\text{H}] = -1.26$ ), as shown in Figure 22.

Here we neglected the effects of unresolved binaries. An et al. (2007b) performed extensive simulations of unresolved binaries in clusters and their influence in the MS-fitting distances. After the same photometric filtering as we applied in this paper, they found that the unresolved binaries can make the MS look brighter by  $\sim 0.007$  mag for a 40% binary fraction<sup>23</sup> because all of the low mass-ratio binaries cannot be detected in the photometric filtering. However, this translates into only  $\sim 0.001$  mag in colors since the slope of the MS is about 5–6. Furthermore, the observed binary fraction of globular clusters is typically less than 20% (e.g., Sollima et al. 2007; Davis et al. 2008, and references therein), which makes the influence of unresolved binaries even smaller.

Figure 23 shows the comparison between the solar-metallicity open cluster M67 CMDs and 3.5 Gyr models at three different metallicities,  $Z = 0.0080$ ,  $0.0190$ , and  $0.0300$  ( $[\text{m}/\text{H}] \approx -0.4, +0.0, +0.2$ ). We used models without convective core overshooting, but the difference from those models based on the overshooting assumption is small in most parts of the CMDs in Figure 23. Near the MS turnoff, the agreement is good between solar-metallicity models and the data. However, the models begin to diverge from the fiducial MS below  $r \sim 16.5$  mag or  $\sim 0.7M_{\odot}$  in their models. The difference becomes as large as  $\sim 0.5$  mag in  $(g-i, r)$  and  $(g-z, r)$  at the bottom of the MS. Users of these models should be warned about this potentially large discrepancy.

#### 5.4. Comparison with Fiducial Sequences in $u'g'r'i'z'$

Clem et al. (2008) observed four globular clusters (M3, M13, M71, M92) and one open cluster (NGC 6791) in the  $u'g'r'i'z'$  passbands with the MegaCam wide-field imager on the Canada-France-Hawaii Telescope. Their data included observations of various integration times, which resulted in highly precise CMDs extending from the tip of the RGB down to approximately four magnitudes below the MS turnoff.

<sup>23</sup> Binary fraction is defined as the number of binaries divided by the total number of systems.

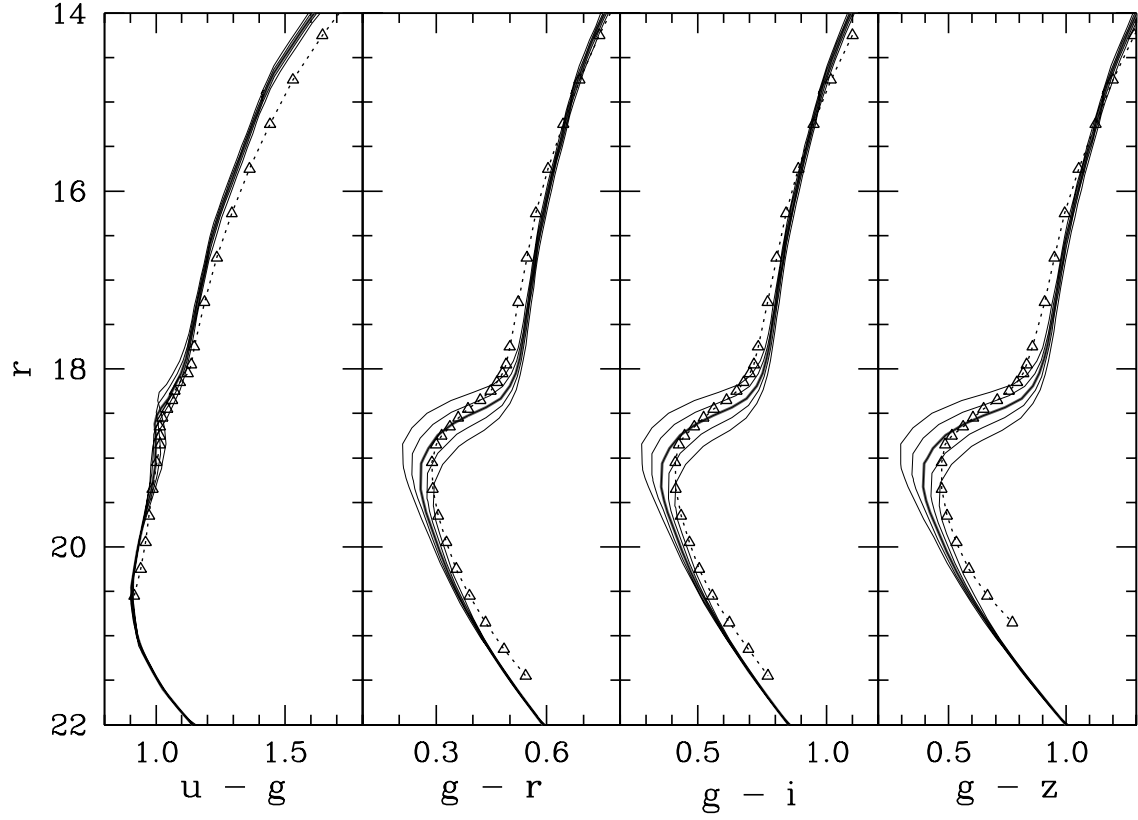


FIG. 18.— Comparisons between fiducial sequences for M15 in this paper (*dotted line with triangles*) and the Girardi et al. theoretical isochrones (*solid lines*). Models are shown with  $Z = 0.0001$  ( $[m/H] \approx -2.3$ ) at ages of 10.0, 11.2, 12.6, 14.1, and 15.9 Gyrs.

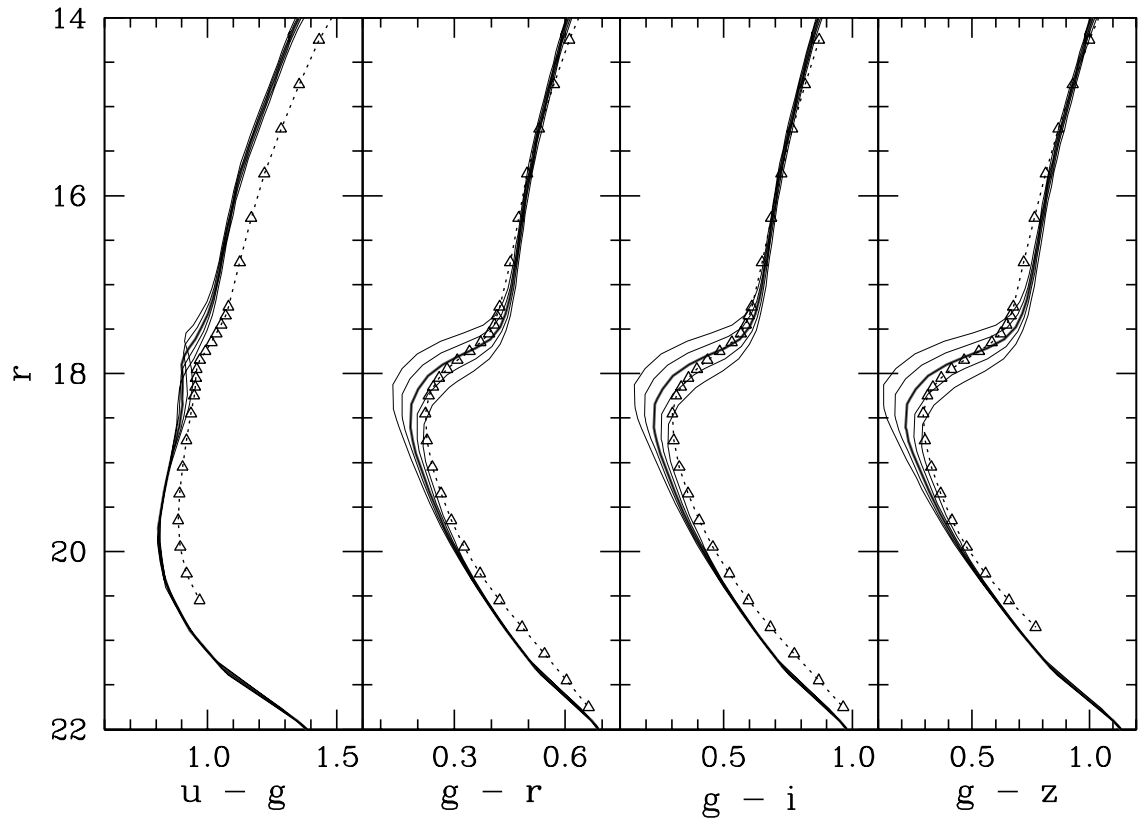


FIG. 19.— Same as in Fig. 18, but for M92.

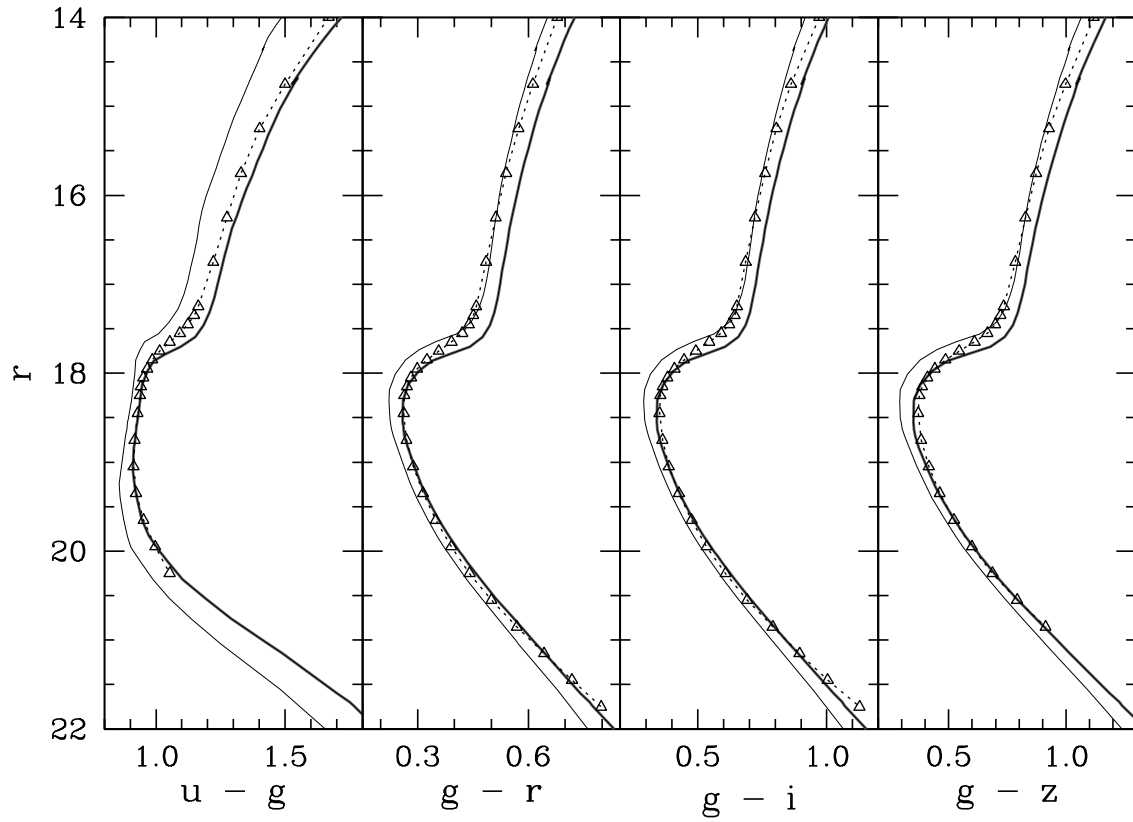


FIG. 20.— Same as in Fig. 18, but for M13. Models are shown for  $Z = 0.0004$  ( $[m/H] \approx -1.7$ ) and  $Z = 0.0010$  ( $[m/H] \approx -1.3$ ) at an age of 12.6 Gyr.

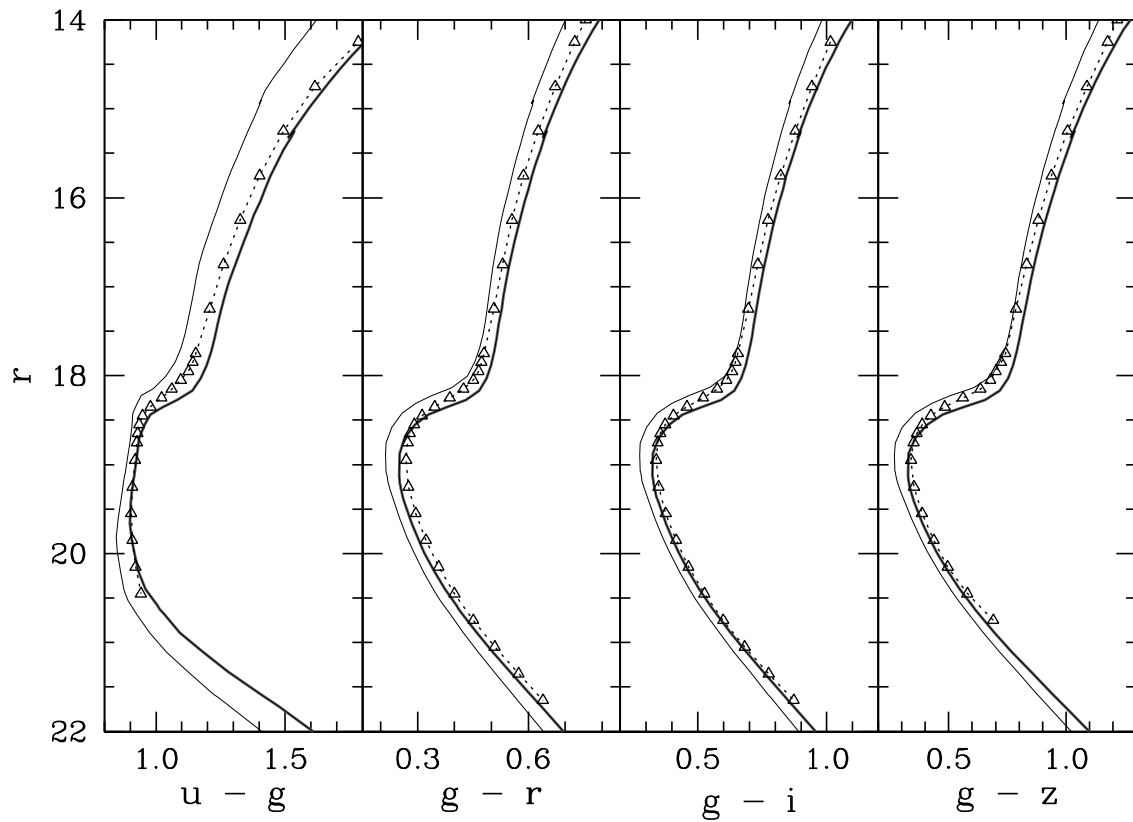


FIG. 21.— Same as in Fig. 20, but for M3.

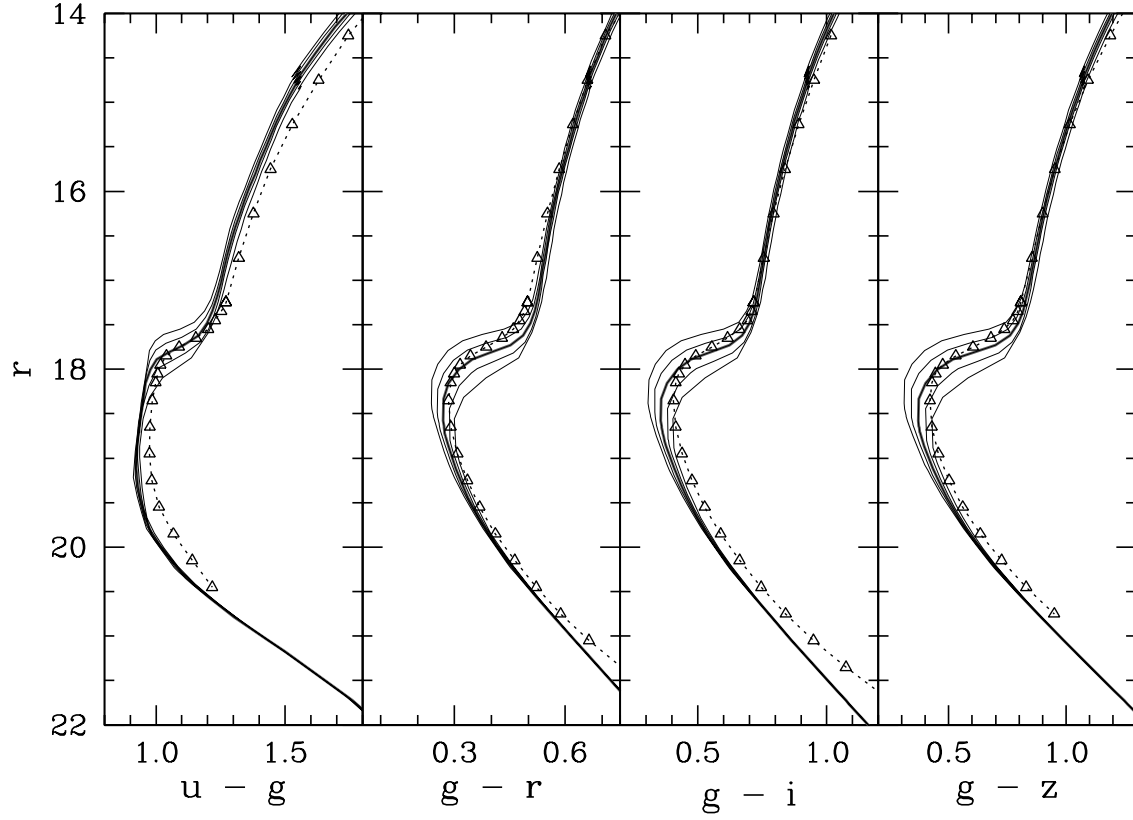


FIG. 22.— Same as in Fig. 18, but for M5. Models are shown for  $Z = 0.0010$  ( $[m/H] \approx -1.3$ ) at ages of 10.0, 11.2, 12.6, 14.1, and 15.9 Gyrs.

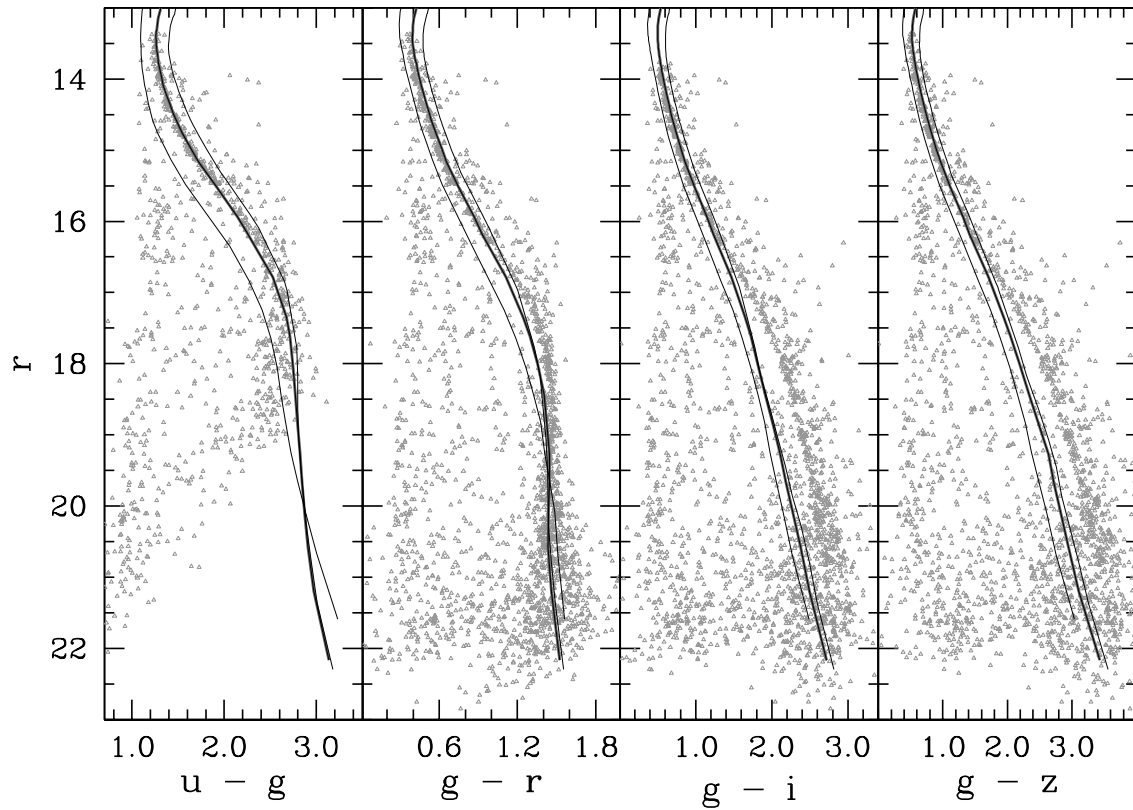


FIG. 23.— Same as in Fig. 18, but for M67. Models are shown for  $Z = 0.0080, 0.0190, \text{ and } 0.0300$  ( $[m/H] \approx -0.4, +0.0, +0.2$ ) at an age of 3.5 Gyr.

The photometry in Clem et al. has been calibrated to the  $u'g'r'i'z'$  system defined by the Smith et al. (2002) sample of standard stars, while the SDSS photometry is on the natural  $ugriz$  system of the 2.5-m survey telescope. Therefore, we converted their fiducial sequences in the  $u'g'r'i'z'$  system onto the SDSS 2.5-m  $ugriz$  system, using the transformation equations in Tucker et al. (2006):  $u = u'$ ,  $g = g' + 0.060[(g' - r') - 0.53]$ ,  $r = r' + 0.035[(r' - i') - 0.21]$ ,  $i = i' + 0.041[(r' - i') - 0.21]$ ,  $z = z' - 0.030[(i' - z') - 0.09]$ . These relations were derived using stars in  $0.70 \leq (u' - g') \leq 2.70$ ,  $0.15 \leq (g' - r') \leq 1.20$ ,  $0.10 \leq (r' - i') \leq 0.60$ , and  $0.20 \leq (i' - z') \leq 0.40$ .

Figures 24 and 25 show comparisons between our fiducial sequences and those in Clem et al. on the  $ugriz$  system. For clarity, comparisons are shown with arbitrary offsets in colors and magnitudes for each cluster. Note that the sequences in Clem et al. extend far beyond the magnitude limits of our fiducial sequences. The comparison in  $g-z$  for M3 is not shown in Figure 24 because the sequence is not available in Clem et al. for that color index. For the same reason, the comparison in  $u-g$  for NGC 6791 is not shown in Figure 25.

While a generally good agreement is found between the two sets of fiducial sequences, the comparisons for M71 show particularly large differences in all four of the color indices. The differences in colors are  $\sim 0.05$ - $0.15$  mag, in the sense that our fiducial sequences are always redder than those in Clem et al. As we noted in § 4.2, the zero points for the M71 photometry were very uncertain, due to the suspicious *Photo* magnitudes in the cluster's flanking field. In addition, the shapes of the fiducial sequences could not be accurately defined due to the strong contamination from background stars. Caution should be given when using our DAOPHOT photometry for M71 and its fiducial sequences.

Except for M71, the differences in colors and/or magnitudes between the two fiducial sequences are typically less than  $\sim 2\%$ . These differences are smaller than those found from the comparison with theoretical isochrones (Figs. 18-23). Furthermore, they are comparable in size to the zero-point errors in the DAOPHOT photometry (§ 4.3). Therefore, the agreement found here not only validates the accuracy of the transformation equations between  $u'g'r'i'z'$  and  $ugriz$ , but also the accuracy of our fiducial sequences derived from the single-epoch photometry.

In the case of NGC 6791, our fiducial sequences on RGB become redder than the Clem et al. sequences at redder colors. The differences at the tip of our fiducial sequences are  $\sim 0.05$ - $0.10$  mag. Although different filter responses can cause these color-dependent zero-point shifts, the observed differences are possibly due to uncertainties in the fiducial sequences from the sparsely populated RGB of the cluster.

## 6. CONCLUSION

We used the DAOPHOT/ALLFRAME suite of programs to derive photometry in  $ugriz$  filter bandpasses for 17 globular clusters and 3 open clusters that have been observed with SDSS. The regions close to the globular clusters are too crowded for the standard SDSS photometric pipeline (*Photo*) to process, and the photometry is not available for the most crowded regions of these clusters. In order to exploit over 100 million stellar objects with  $r < 22.5$  mag observed by SDSS, we used the DAOPHOT crowded field photometry package to derive accurate magnitudes and colors of stars in the Galactic clusters. We also derived fiducial sequences for the 20 clusters on the native SDSS 2.5-meter  $ugriz$  photometric system, which can be directly applied to the SDSS photometry with-

out relying upon transformations from the  $u'g'r'i'z'$  system.

We showed that DAOPHOT PSF magnitudes are spatially and temporally uniform to  $\lesssim 0.5\%$  with respect to aperture photometry. However, comparison between the DAOPHOT and the *Photo* magnitudes showed  $\sim 2\%$  high spatial frequency structures on a sub-field scale, indicating an error in the *Photo* magnitudes. Although the 2% accuracy of *Photo* magnitudes already makes SDSS one of the most successful optical surveys, our result indicates that its photometric accuracy could be further improved in the future (e.g., Ivezić et al. 2007; Padmanabhan et al. 2008). Nevertheless, the accuracy of the zero point in the DAOPHOT photometry is predominantly limited by the  $\sim 2\%$  run-to-run zero-point variations.

From repeated flux measurements in overlapping strips/runs, we also measured realistic photometric errors for SDSS photometry determined by DAOPHOT. The error distributions at the bright ends indicate errors of  $\sim 1\%$  in  $griz$  and  $\sim 2\%$  in the  $u$  band, which are a factor of two better than the 2% rms photometric precision obtained with *Photo* (Ivezić et al. 2003). We found slightly larger rms differences ( $\sim 0.025$  mag) between the *Photo* and the DAOPHOT magnitudes in semi-crowded open cluster fields.

Using fiducial sequences, we performed a preliminary test of theoretical isochrones from Girardi et al. (2004). We found that model colors differ by  $\sim 0.02$ - $0.05$  mag from those of the fiducial sequences for our adopted cluster distance and reddening values. Furthermore, these models cannot be simultaneously matched to the MS and RGB ridgelines of our fiducial sequences. In the solar-metallicity open cluster M67, model colors are too blue by  $\sim 0.5$  mag at the bottom of the MS. On the other hand, we found a good agreement ( $\lesssim 0.02$  mag in colors) with the Clem et al. (2008) empirical fiducial sequences in  $u'g'r'i'z'$ , after transformation to the native  $ugriz$  system using the transformation equations of Tucker et al. (2006). This result not only validates the accuracy of the transformation equations between  $u'g'r'i'z'$  and  $ugriz$ , but also the accuracy of our fiducial sequences derived from the single-epoch photometry.

There are several projects that will benefit from our accurate cluster photometry and fiducial sequences in  $ugriz$ . The photometry is of great value for empirical calibrations of the spectroscopic measurements such as the SEGUE Stellar Parameter Pipeline (Lee et al. 2007a,b; Allende Prieto et al. 2007), and for deriving accurate transformations between  $ugriz$  and other photometric systems. As templates for stellar populations, fiducial sequences can be used to identify and characterize the dwarf companions to the Milky Way and Andromeda galaxies. They can be also used for tracing the tidal structures from globular clusters (e.g., Odenkirchen et al. 2001). In addition, the distances to individual stars in SDSS can be better determined with  $ugriz$  fiducials of well-studied clusters, which is the subject of the next paper in this series.

D.A. and J.A.J. thank Donald Terndrup, Marc Pinsonneault, and Andrew Gould for helpful comments. D.A. and J.A.J. acknowledge support from SSP-271. H.L.M. acknowledges support from NSF grants AST-0098435 and AST-0607518.

Funding for the SDSS and SDSS-II has been provided by the Alfred P. Sloan Foundation, the Participating Institutions, the National Science Foundation, the U.S. Department of Energy, the National Aeronautics and Space Administration, the Japanese Monbukagakusho, the Max Planck Society, and the Higher Education Funding Council for England. The SDSS

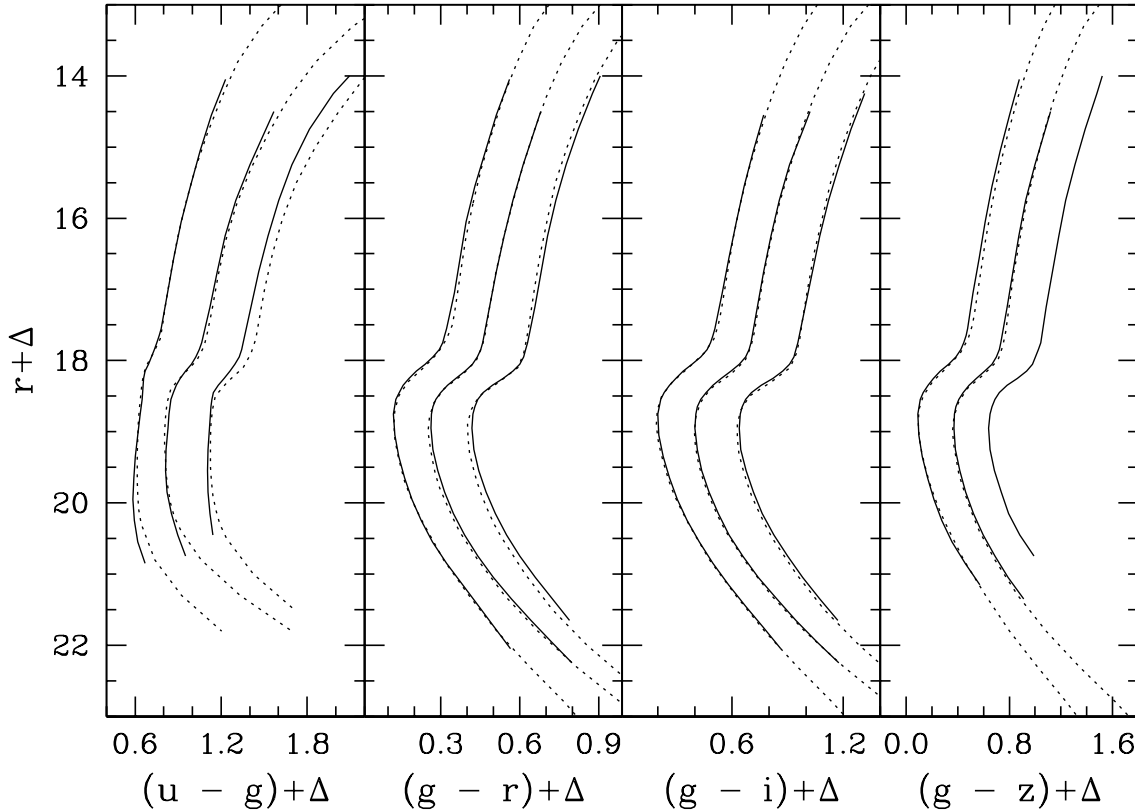


FIG. 24.— Comparisons between fiducial sequences in this paper (*solid line*) and those in Clem et al. (*dotted line*), after transforming the latter from the  $u'g'r'i'z'$  to the  $ugriz$  system. Fiducial sequences are shown for M92, M13, and M3 (from *left to right*) with arbitrary offsets in colors and magnitudes for clarity. The comparison in  $g-z$  for M3 is not shown because the sequence is not available in Clem et al. for that color index.

Web Site is <http://www.sdss.org/>.

The SDSS is managed by the Astrophysical Research Consortium for the Participating Institutions. The Participating Institutions are the American Museum of Natural History, Astrophysical Institute Potsdam, University of Basel, University of Cambridge, Case Western Reserve University, University of Chicago, Drexel University, Fermilab, the Institute for Advanced Study, the Japan Participation Group, Johns Hopkins University, the Joint Institute for Nuclear Astro-

physics, the Kavli Institute for Particle Astrophysics and Cosmology, the Korean Scientist Group, the Chinese Academy of Sciences (LAMOST), Los Alamos National Laboratory, the Max-Planck-Institute for Astronomy (MPIA), the Max-Planck-Institute for Astrophysics (MPA), New Mexico State University, Ohio State University, University of Pittsburgh, University of Portsmouth, Princeton University, the United States Naval Observatory, and the University of Washington.

#### REFERENCES

- Abazajian, K., et al. 2003, *AJ*, 126, 2081  
 Abazajian, K., et al. 2004, *AJ*, 128, 502  
 Abazajian, K., et al. 2005, *AJ*, 129, 1755  
 Adelman-McCarthy, J. K., et al. 2006, *ApJS*, 162, 38  
 Adelman-McCarthy, J. K., et al. 2007, *ApJS*, 172, 634  
 Adelman-McCarthy, J. K., et al. 2008, *ApJS*, 175, 297  
 Allende Prieto, C., Beers, T. C., Wilhelm, R., Newberg, H. J., Rockosi, C. M., Yanny, B., & Lee, Y. S. 2006, *ApJ*, 636, 804  
 Allende Prieto, C., et al. 2007, *ArXiv e-prints*, 710, arXiv:0710.5780  
 An, D., Terndrup, D. M., & Pinsonneault, M. H. 2007a, *ApJ*, 671, 1640  
 An, D., Terndrup, D. M., Pinsonneault, M. H., Paulson, D. B., Hanson, R. B., & Stauffer, J. R. 2007b, *ApJ*, 655, 233  
 Anthony-Twarog, B. J., Tanner, D., Cracraft, M., & Twarog, B. A. 2006, *AJ*, 131, 461  
 Belokurov, V., et al. 2006, *ApJ*, 642, L137  
 Bessell, M. S., Castelli, F., & Plez, B. 1998, *A&A*, 333, 231  
 Carraro, G., Villanova, S., Demarque, P., McSwain, M. V., Piotto, G., & Bedin, L. R. 2006, *ApJ*, 643, 1151  
 Cassisi, S., Salaris, M., Castelli, F., & Pietrinferni, A. 2004, *ApJ*, 616, 498  
 Castelli, F., Gratton, R. G., & Kurucz, R. L. 1997, *A&A*, 318, 841  
 Clem, J. L., Vanden Berg, D. A., & Stetson, P. B. 2008, *AJ*, 135, 682  
 Coleman, M. G., Jordi, K., Rix, H.-W., Grebel, E. K., & Koch, A. 2007, *AJ*, 134, 1938  
 Davenport, J. R. A., Bochanski, J. J., Covey, K. R., Hawley, S. L., West, A. A., & Schneider, D. P. 2007, *AJ*, 134, 2430  
 Davis, D. S., Richer, H. B., Anderson, J., Brewer, J., Hurley, J., Kalirai, J. S., Rich, R. M., & Stetson, P. B. 2008, *AJ*, 135, 2155  
 de Jong, J. T. A., Rix, H.-W., Martin, N. F., Zucker, D. B., Dolphin, A. E., Bell, E. F., Belokurov, V., & Evans, N. W. 2008, *AJ*, 135, 1361  
 Eisenstein, D. J., et al. 2006, *ApJS*, 167, 40  
 Fukugita, M., Ichikawa, T., Gunn, J. E., Doi, M., Shimasaku, K., & Schneider, D. P. 1996, *AJ*, 111, 1748  
 Girardi, L., Bressan, A., Bertelli, G., & Chiosi, C. 2000, *A&AS*, 141, 371  
 Girardi, L., Grebel, E. K., Odenkirchen, M., & Chiosi, C. 2004, *A&A*, 422, 205  
 Gratton, R., Bragaglia, A., Carretta, E., & Tosi, M. 2006, *ApJ*, 642, 462  
 Gratton, R. G., Fusi Pecci, F., Carretta, E., Clementini, G., Corsi, C. E., & Lattanzi, M. 1997, *ApJ*, 491, 749  
 Gunn, J. E., et al. 1998, *AJ*, 116, 3040  
 Gunn, J. E., et al. 2006, *AJ*, 131, 2332  
 Harris, W. E. 1996, *AJ*, 112, 1487  
 Hogg, D. W., Finkbeiner, D. P., Schlegel, D. J., & Gunn, J. E. 2001, *AJ*, 122, 2129  
 Holberg, J. B., & Bergeron, P. 2006, *AJ*, 132, 1221  
 Ivezić, Ž., et al. 2001, *AJ*, 122, 2749  
 Ivezić, Ž., et al. 2003, *Memorie della Societa Astronomica Italiana*, 74, 978  
 Ivezić, Ž., et al. 2004, *Astronomische Nachrichten*, 325, 583  
 Ivezić, Ž., et al. 2007, *AJ*, 134, 973  
 Johnson, H. L. 1957, *ApJ*, 126, 121  
 Jurić, M., et al. 2008, *ApJ*, 673, 864  
 Kaiser, N., et al. 2002, *Proc. SPIE*, 4836, 154  
 Kim, Y.-C., Demarque, P., Yi, S. K., & Alexander, D. R. 2002, *ApJS*, 143, 499

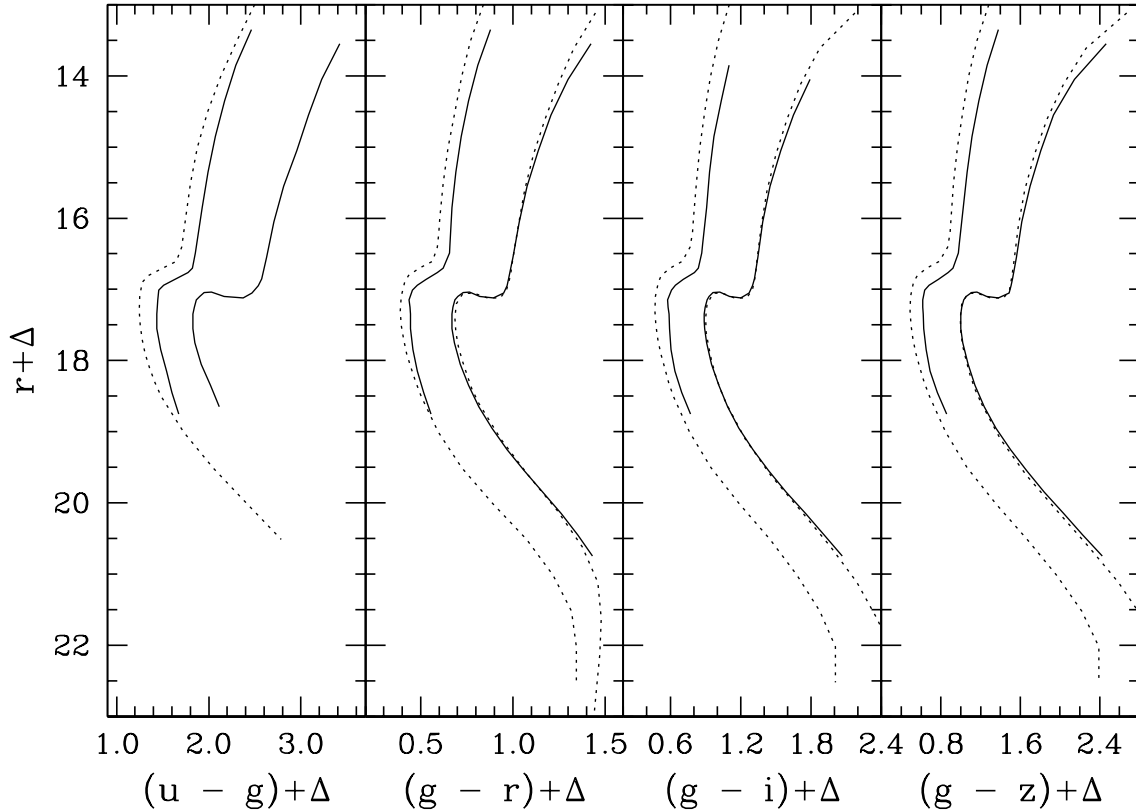


FIG. 25.— Same as in Fig. 24, but for M71 (*left*) and NGC 6791 (*right*). See text for a discussion on the M71 comparisons. The comparison in  $u-g$  for NGC 6791 is not shown because the sequence is not available in Clem et al. for that color index.

- Kraft, R. P. 1994, *PASP*, 106, 553  
 Kraft, R. P., & Ivans, I. I. 2003, *PASP*, 115, 143  
 Kraft, R. P., & Ivans, I. I. 2004, in *Carnegie Observatories Astrophysics Ser. 4: Origin and Evolution of the Elements, 2004*, ed. A. McWilliam & M. Rauch (Pasadena: Carnegie Observatories), <http://www.ocivw.edu/ocivw/symposia/series/symposium4/proceedings.html>  
 Lee, Y. S., et al. 2007a, *ArXiv e-prints*, 710, arXiv:0710.5645  
 Lee, Y. S., et al. 2007b, *ArXiv e-prints*, 710, arXiv:0710.5778  
 Lupton, R. H., Gunn, J. E., & Szalay, A. S. 1999, *AJ*, 118, 1406  
 Lupton, R. H., Ivezić, Z., Gunn, J. E., Knapp, G., Strauss, M. A., & Yasuda, N. 2002, *Proc. SPIE*, 4836, 350  
 Newberg, H. J., et al. 2002, *ApJ*, 569, 245  
 Odenkirchen, M., et al. 2001, *ApJ*, 548, L165  
 Oke, J. B., & Gunn, J. E. 1983, *ApJ*, 266, 713  
 Origlia, L., Valentí, E., Rich, R. M., & Ferraro, F. R. 2006, *ApJ*, 646, 499  
 Padmanabhan, N., et al. 2008, *ApJ*, 674, 1217  
 Perryman, M. A. C., et al. 2001, *A&A*, 369, 339  
 Pier, J. R., Munn, J. A., Hindsley, R. B., Hennessy, G. S., Kent, S. M., Lupton, R. H., & Ivezić, Ž. 2003, *AJ*, 125, 1559  
 Pinsonneault, M. H., Terndrup, D. M., Hanson, R. B., & Stauffer, J. R. 2003, *ApJ*, 598, 588  
 Pinsonneault, M. H., Terndrup, D. M., Hanson, R. B., & Stauffer, J. R. 2004, *ApJ*, 600, 946  
 Reid, I. N. 1997, *AJ*, 114, 161  
 Salaris, M., Chieffi, A., & Straniero, O. 1993, *ApJ*, 414, 580  
 Schechter, P. L., Mateo, M., & Saha, A. 1993, *PASP*, 105, 1342  
 Schlegel, D. J., Finkbeiner, D. P., & Davis, M. 1998, *ApJ*, 500, 525  
 Sesar, B., et al. 2006, *AJ*, 131, 2801  
 Smith, J. A., et al. 2002, *AJ*, 123, 2121  
 Smolčić, V., Zucker, D. B., Bell, E. F., Coleman, M. G., Rix, H. W., Schinnerer, E., Ivezić, Ž., & Kniazev, A. 2007, *AJ*, 134, 1901  
 Snenen, C., Kraft, R. P., Guhathakurta, P., Peterson, R. C., & Fulbright, J. P. 2004, *AJ*, 127, 2162  
 Sollima, A., Beccari, G., Ferraro, F. R., Fusi Pecci, F., & Sarajedini, A. 2007, *MNRAS*, 380, 781  
 Stetson, P. B. 1987, *PASP*, 99, 191  
 Stetson, P. B. 1990, *PASP*, 102, 932  
 Stetson, P. B. 1994, *PASP*, 106, 250  
 Stetson, P. B., Bruntt, H., & Grundahl, F. 2003, *PASP*, 115, 413  
 Stoughton, C., et al. 2002, *AJ*, 123, 485  
 Stubbs, C. W., Sweeney, D., Tyson, J. A., & LSST 2004, *Bulletin of the American Astronomical Society*, 36, 1527  
 Tucker, D. L., et al. 2006, *Astronomische Nachrichten*, 327, 821  
 Venn, K. A., Irwin, M., Shetrone, M. D., Tout, C. A., Hill, V., & Tolstoy, E. 2004, *AJ*, 128, 1177  
 York, D. G., et al. 2000, *AJ*, 120, 1579